PART II

External Factors

CHAPTER

4

Propagation Effects and Mechanisms

Jay A. Saffold

Chapter Outline

4.1 INTRODUCTION

This chapter discusses the effects of the transmission medium on the propagation of electromagnetic waves traveling from a radar transmitter to a target and back to the receiver. Many factors can influence the propagating radar signal, such as the composition of the atmosphere, clouds, rain, insects, and obstacles. The wave will also be affected by the ground the wave passes over as well as other topological features, such as hills, valleys, and lakes. This chapter considers only how these topological features affect the propagating wave, while the radar return from these features, known as clutter, are discussed in the next chapter.

The effect of the propagation medium can be described as a series of mechanisms whose impact may be combined through superposition. Several of these mechanisms can exist simultaneously. Some of the major propagation mechanisms and general guidelines for assessing the primary sources of propagation impact on an application are as follows:

- *Atmospheric absorption* increases with higher frequency, longer ranges, and higher concentration of atmospheric particles (e.g., water, fog, snow, smoke).

- *Atmospheric refraction* anomalies (surface ducts), which tend to generally be less significant at higher frequencies, occur more often in conditions of high humidity, at land/sea boundaries, and at night when a thermal profile inversion exists.
- *Atmospheric volumetric scattering* increases with higher frequency, larger suspended particle sizes, and higher concentrations of atmospheric particles (e.g., water, fog, snow, smoke) and can be a strong function of wave polarization and frequency.
- *Atmospheric turbulence* is generally a high-frequency (HF) phenomenon (e.g., optical, millimeter wave [MMW], or sub-MMW) and is strongly dependent on refractive index (or temperature) variations and winds.
- *Surface diffraction* effects tend to increase with lower-frequency and higher-surface root mean square (rms) roughness specification. The effect of the earth's surface features can be roughly separated into two regions of influence: the interference region and the diffraction region (defined in Section 4.3.2)
- *Surface multipath* effects occur in the interference region and tend to increase with lower-frequency and lower-surface rms roughness specifications. Multipath forward scattering is generally confined to terrain- and target-bounced reflections in the direction of the receiver.
- *Surface intervisibility* effects (shadowing) tend to increase with higher-surface roughness specifications and lower link altitudes. Intervisibility is also affected by the presence of clutter *discretes* (specific, isolated, strong clutter scatterers) and the spherical (or effective) Earth horizon boundary limitations.

The atmospheric mechanisms of absorption, refraction, scattering, and turbulence are collectively referred to as *atmospherics*. In general, all mechanisms are present in the intermediate path for the propagating wave in the real world. In this chapter, the physics and significance of each mechanism are discussed.

4.2 PROPAGATION FACTOR

The impact of propagation mechanisms can be applied to the free-space radar range equation as a "gain" or "loss" factor. Specifically, the peak amplitude, E_0', of the one-way received electric field vector in the presence of propagation effects is related to the amplitude that would be received in free-space propagation without these effects, E_0, according to

$$\begin{aligned} E_0' &= F_v E_0 \\ &= (F e^{j\phi_F}) E_0 \end{aligned} \tag{4.1}$$

where F_v is the complex voltage *propagation factor*, F is its magnitude, and ϕ_F is its phase. F_v is composed of several component factors,

$$F_v = F_{v_1} \cdot F_{v_2} \cdot F_{v_3} \cdot \ldots \cdot F_{v_N} \tag{4.2}$$

Thus,

$$\begin{aligned} F &= F_1 \cdot F_2 \cdot F_3 \cdot \ldots \cdot F_N \\ \phi_F &= \phi_{F_1} + \phi_{F_2} + \phi_{F_3} + \ldots + \phi_{F_N} \end{aligned} \tag{4.3}$$

Since power is proportional to $|E|^2$, the propagation factor applicable to one-way received power is

$$|F_v|^2 = F^2 \tag{4.4}$$

Many texts discuss only this power form of the propagation factor.

Often the effect of propagation mechanisms on two-way propagation is needed. The fundamental assumption for two-way data is that propagation effects are path-reciprocal so that the two-way propagation factor is simply the one-way factor squared.

$$F_v^2 = F^2 e^{j2\phi_F} \tag{4.5}$$

The monostatic radar range equation of Chapter 1 then becomes

$$P_r = \frac{P_t G^2 \lambda^2 \sigma}{(4\pi)^3 L_s R^4} F^4 \tag{4.6}$$

Caution is needed in determining whether published data is based on one-way or two-way propagation. Care must also be taken not to confuse propagation factor and noise figure, since both are commonly represented by the symbol F.

4.3 PROPAGATION PATHS AND REGIONS

4.3.1 Monostatic and Bistatic Propagation

Most radio, cellular, and wireless communications links are concerned only with one-way propagation. Radar is generally concerned with two-way propagation between the transmitter and receiver. If the receiver is colocated with the transmitter (as is often the case), this is called a two-way *monostatic* case. The main difference from the communications case is that any propagation effects will be more impactive since the radar wave passes through the medium twice. Cases where the transmitter and receiver are not colocated are *bistatic*. Here, the main consideration from a propagation standpoint is that the radar wave may pass through two different propagation paths, unless the bistatic angle is relatively narrow or the target is not at a great distance. While much less common than monostatic radar, bistatic systems are not unusual. Figure 4-1 illustrates these three classes of propagation paths.

4.3.2 The Surface

Every obstacle within an expanding wave's path will impede direct propagation to an observer near the earth. Simple ray tracing illustrates the *line-of-sight* (LOS) region, also

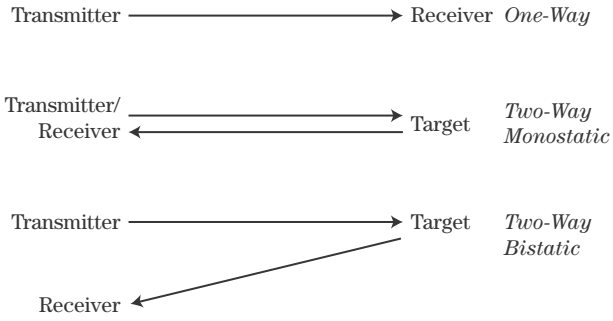

FIGURE 4-1 ■ Three classes of propagation paths.

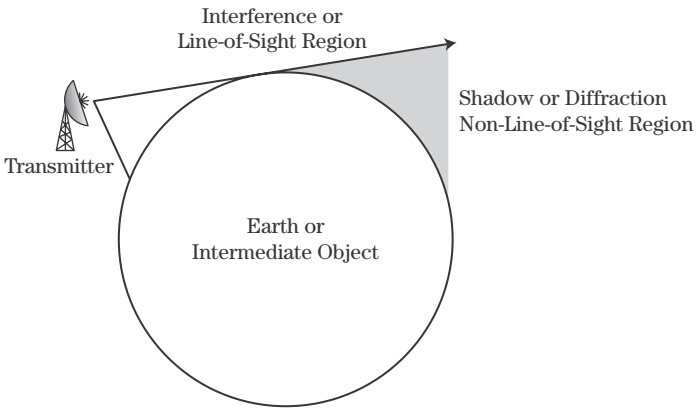

FIGURE 4-2 ■ Regions defined by the LOS propagation path near the earth's surface.

called the *interference* region, and the non-line-of-sight (*shadow* or *diffraction*) region associated with a transmitter above the surface of the earth. These regions are illustrated in Figure 4-2. A diffraction or refraction mechanism is necessary for electromagnetic (EM) waves to propagate into the shadow region.[1]

Two points in space are said to be *intervisible* with one another if there is an uninterrupted line of sight between them. In general, the rougher the surface, the higher the number of ground points that will not be visible to a given emitter (and vice versa). Clearly, local geometry and discrete location play a significant role in intervisibility estimation [1].

4.3.3 The Atmosphere

For the purposes of radar propagation analysis, the atmosphere can be characterized by a number of key radial layers. Propagation of the radiated wave is affected by the composition of these layers as well as the boundaries or interfaces between these layers according to the properties of both the wave and the boundary itself. Figure 4-3 illustrates some of the key layers associated with the atmosphere and their general altitude above sea level on the earth.

These layers can be characterized by the vertical distribution of temperature fluctuations, as illustrated in Figure 4-3, as well as the water vapor in the layer. The principal layers are the troposphere, stratosphere, mesosphere, and the thermosphere.

The *troposphere,* the region in contact with the earth, is the lowest layer of the atmosphere and extends from the earth's surface to a height of 10 to 16 km. Four fifths of the mass of the atmosphere is contained in this layer, which is characterized by a decreasing temperature as height increases in the vertical plane. The rate of decrease for this temperature, based on the 1976 U.S. Standard Atmosphere, is about 6.5 °C/km above ground level. Most weather processes (and water vapor) occur in this atmospheric layer. The *stratosphere* is the layer of the atmosphere extending above the tropopause to a height of about 55 km. Very little weather occurs in this layer due to a low water vapor content. The *mesosphere* is the atmospheric layer between the stratopause and the mesopause. Like the

[1]Of course, scattering from an LOS ray from another obstacle can cause multibounce rays to propagate into a shadow zone. This multibounce phenomenon tends to be more significant in one-way propagation (or bistatic) radar geometries.

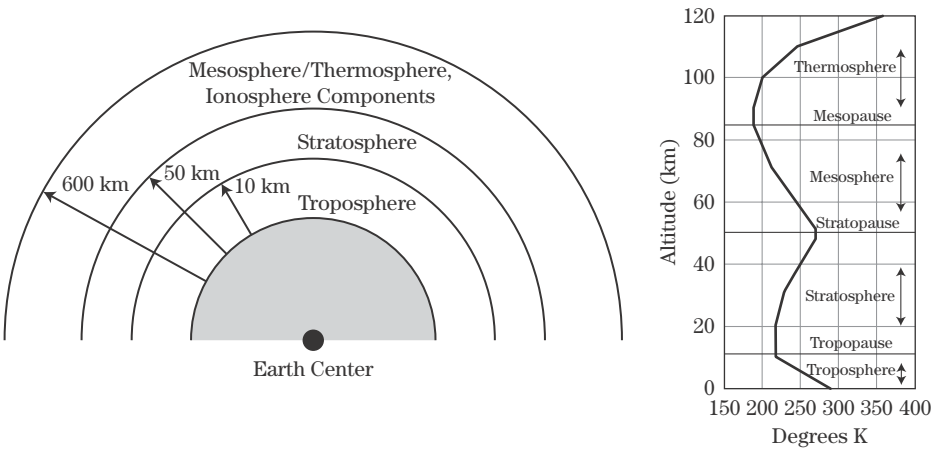

FIGURE 4-3 ■ Rays propagating through atmospheric regions. (From Eaves et al. [2] and Bogush [3]. With permission.)

troposphere, it is a layer where the temperature decreases with height. Special features of the mesosphere include a region of extremely strong winds centered near heights of 65 km.

The *thermosphere* is a high-temperature region extending upward from heights of about 80 km to the outer reaches of the atmosphere. The thermosphere contains the majority of the ionosphere, with colorful auroras often in this region. The *ionosphere* is an upper region of the earth's atmosphere in which many of the atmospheric atoms and molecules have become electrically charged by the addition or removal of electrons to produce ions. Relative to the layered regions of the atmosphere, the ionosphere begins at a base near the stratopause, rising through the mesosphere to a peak in the thermosphere. The ionosphere is subdivided into (in order of increasing altitude) the D layer, E layer, F1 layer, and F2 layer. At night the D layer vanishes, and the F1 and F2 layers merge into a single layer.

Ionization in the F2 region, primarily caused by the solar flux and cosmic radiation, serves as a low-attenuation reflector for long-wave radio signals by day. This layer has long been exploited for stable communication over long distances. For example, transoceanic navigation by ships and aircraft is accomplished with the aid of this region's reflection and attenuation properties. This is also the basis of the concept of over-the-horizon (OTH) radar used for very long-range ground-based surveillance and tracking systems, as discussed later in this chapter. See Section 4.7 for additional discussion of the ionosphere.

4.4 | ATMOSPHERIC ATTENUATION AND ABSORPTION

The *attenuation* of an EM wave through an atmosphere is caused by two major components: absorption and scattering. Absorption occurs when the atmosphere contains gases or particulates with lossy properties (e.g., oxygen molecules or raindrops). Some of the EM wave's energy is then lost to heat within the lofted particle. Scattering occurs when the particulate is of sufficient size to cause some of the wave to be reflected in directions away from the collecting receiver. The magnitude of both phenomena is a direct function of the particulate density along the EM wave propagation path.

Since atmospheric effects are volume phenomena, the potential exists for some level of scattering off the volume boundary and from the internal particles themselves, as shown

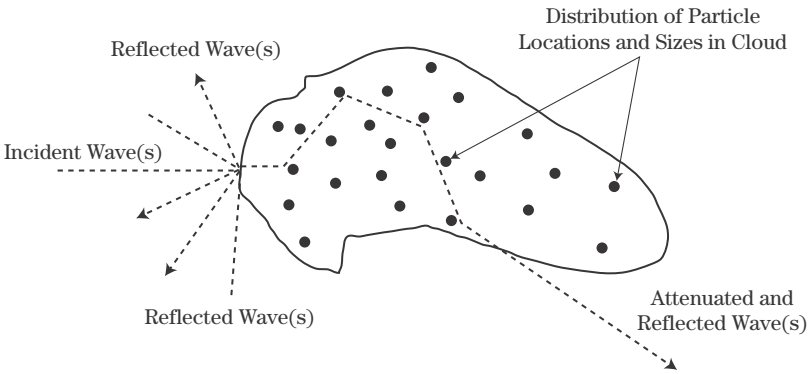

FIGURE 4-4 ■ Attenuation due to wave scattering and absorption by particulates.

in Figure 4-4. Additional scattering can also be caused by the presence of other objects in the atmosphere such as heavy dust, insects, and birds. Scattering from precipitation or other suspended particulates is an important component of total attenuation for a radar link. Further information, which can be used within this methodology, regarding volume scattering from sources other than precipitants can be found in, for example, [4,5]. Atmospheric particle scattering is generally isotropic and increases with frequency and suspended particle size and conductivity.[2] It has been shown that volumetric scattering is a strong function of incident polarization, frequency, and precipitation rates or particle concentrations.

Thus, the wave incident upon the particulate cloud will be both scattered and absorbed according to the particulate size, lossy dielectric properties, and density within the signal path. Only that signal component scattered in the direction of the collecting receiver will be measured. The ratio of the power of the one-way attenuated wave, A, to the free-space wave, A_0, defines the atmospheric loss (attenuation) in the path:

$$F^2 = \frac{A}{A_0} \tag{4.7}$$

In general, one-way attenuation of radar signals in the atmosphere can be expressed in the form

$$F^2 = 10^{\alpha L/2} \tag{4.8}$$

where α is the attenuation coefficient in units of meter^{-1} for the atmospheric type and density, and L is the path length in meters. In many references, the attenuation coefficient is given as a two-way value—hence the factor of $1/2$ in the exponent. For cases in which the α is expressed in dB/km, the one-way propagation factor can be expressed in dB as

$$F^2\ (\text{dB}) = \frac{\alpha L}{2} \tag{4.9}$$

with L (one-way propagation distance) expressed in kilometers.

For longer-range applications, the atmospheric content can be considered heterogeneous, as suggested by Figure 4-5. Using superposition, the impacts of each can be "summed" according to type, density, and path length occupancy, L_n, within the total

[2]Particles that are extremely small compared with a wavelength will scatter more isotropically.

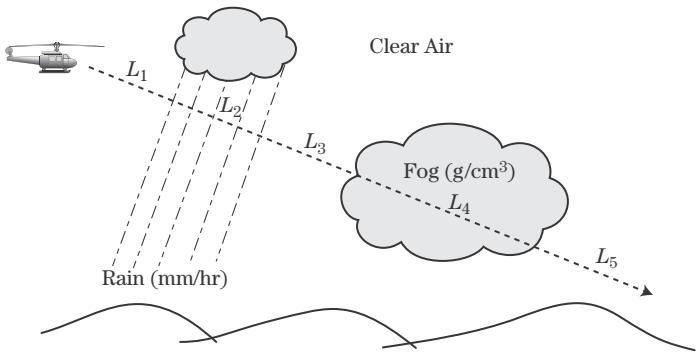

FIGURE 4-5 ■ Heterogeneous atmosphere impacts.

signal path to get the total one-way propagation factor:

$$F^2 = \frac{A}{A_0} = 10^{\alpha_1 L_1/2} \cdot 10^{\alpha_2 L_2/2} \cdot \ldots \cdot 10^{\alpha_N L_N/2} \tag{4.10}$$

Propagating waves within the troposphere will suffer some atmospheric loss due to the presence of oxygen and water vapor in the atmosphere. Other than man-made conditions, the presence of both free molecules and suspended particles such as dust grains, frozen precipitants, and water drops that condense in fog and rain are the primary absorption mechanisms. When no condensation is present (clear air conditions), the absorption is due to oxygen and water vapor molecules. Recognizing that atmospheric factors are a strong function of time, a frequency of occurrence is often used in evaluating atmospheric attenuation. For many missions atmospheric attenuation is one of the most prominent mechanisms affecting radar system performance.

Table 4-1 summarizes typical one-way loss coefficients expected for X-band (10 GHz) propagation though different atmospheric types. The factors determining the attenuation coefficient for each of these conditions are described in the following subsections. These data, derived from multiple references cited in the appropriate sections, can be used to predict the path attenuation for arbitrary path lengths.

TABLE 4-1 ■ Typical One-Way Attenuation Coefficients, α, for Some Selected Atmospherics at 10 GHz

Description	Attenuation Coefficient (dB/km)	Water Content (g/m^3)	Remarks
Clear air	0.01	7.5	Based on sea-level elevation, 42% relative humidity, and 20°C temperature
Dust	0.004	0.1	Based on sea-level elevation, 0 relative humidity, and 20°C temperature
Radiation fog	0.0688	0.1	Based on sea-level elevation, 100% relative humidity, and 20°C temperature
Fog oil (Engine smoke)	0.43	0.0001	Based on sea-level elevation, 0 relative humidity, and 20°C temperature
Rain (4 mm/hr) (10 mm/hr)	0.05 0.17	n/a[1]	Based on sea-level elevation, 100% relative humidity, and 20°C temperature
Snow (2 mm/hr)	0.0016	n/a[1]	Based on sea-level elevation, 100% relative humidity, and 0°C temperature
Special smokes and obscurants	8.6	0.001	Based on sea-level elevation, 0 relative humidity, and 20°C temperature

[1] Attenuation coefficients for rain and snow are based primarily on fall rate in this attenuation model.

4.4.1 Clear Air Water Vapor

In general, free space does not exist in the real world. Propagation under ideal conditions in the atmosphere will include attenuation due to water vapor, oxygen, and other normal particulates. Figure 4-6a shows the atmospheric attenuation for two temperatures at sea level, 59% relative humidity, and standard atmospheric pressure of 1013.25 kPa, and Figure 4-6b compares attenuation at two different altitudes.

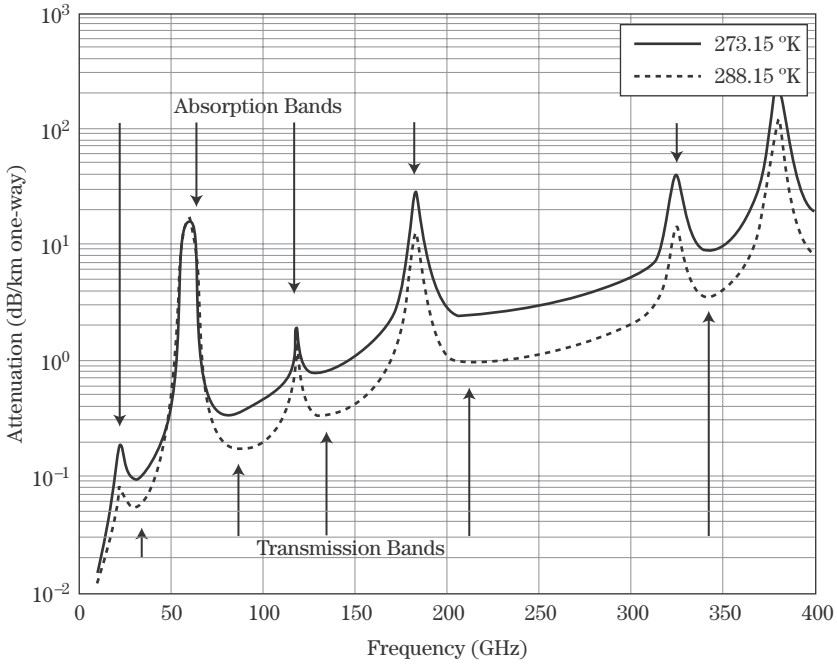

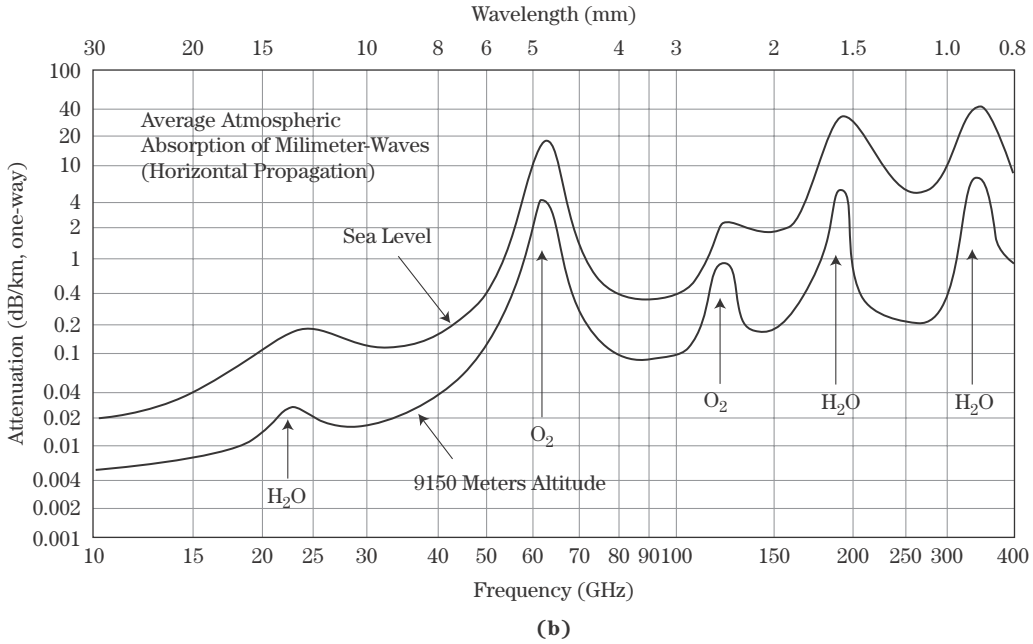

FIGURE 4-6 ■ Attenuation coefficient due to atmospheric gases and water vapor. (a) Variation with temperature. (Courtesy of Bruce Wallace, MMW Concepts. With permission.) (b) Variation with altitude. (From P-N Designs, Inc. [6].)

The dips in attenuation are typically called *transmission bands*, and the peaks are known as *absorption bands*. Radar range can be maximized by operating at a transmission-band frequency. Absorption-band frequencies are useful for applications where the designer wants the signal to reach its desired destination but also is trying to minimize the chance of it reaching farther, to undesired locations.

4.4.2 Rain

Rain is generally characterized by a fall rate, typically in millimeters per hour, known as the *rain rate*. The attenuation due to rain is a function of the rain rate and the drop-size distribution model, which differs in different areas in the world. A general model to estimate the one-way attenuation α in dB/km is given by

$$\alpha = a \cdot r^b \tag{4.11}$$

where a and b are constants based on drop-size distribution model (rain type and geographical region), temperature, frequency, and polarization, and r is the rainfall rate in mm/hr.

Polarimetric attenuation sensitivity for rain occurs where the particulate drops are aspherical and thus have preferred polarization characteristics. Numerous references indicate rain attenuation coefficients; however, only a limited amount of polarimetric data are available. Table 4-2 gives values of a and b as a function of polarization (vertical or

TABLE 4-2 ■ Summary of Empirical Coefficients for Rain Attenuation Model at Linear V, H Polarization

Frequency (GHz)	a_h	a_v	b_h	b_v
1	0.0000387	0.0000352	0.912	0.880
2	0.000154	0.000138	0.963	0.923
3	0.000650	0.000591	1.121	1.075
6	0.00175	0.00155	1.308	1.265
7	0.00301	0.00265	1.332	1.312
8	0.00454	0.00395	1.327	1.310
10	0.0101	0.00887	1.276	1.264
12	0.0188	0.0168	1.217	1.200
15	0.0367	0.0347	1.154	1.128
20	0.0751	0.0691	1.099	1.065
25	0.124	0.113	1.061	1.030
30	0.187	0.167	1.021	1.000
35	0.263	0.233	0.979	0.963
40	0.350	0.310	0.939	0.929
45	0.442	0.393	0.903	0.897
50	0.536	0.479	0.873	0.868
60	0.707	0.642	0.826	0.824
70	0.851	0.784	0.793	0.793
80	0.975	0.906	0.769	0.769
90	1.06	0.999	0.753	0.754
100	1.12	1.06	0.743	0.744
120	1.18	1.13	0.731	0.732
150	1.31	1.27	0.710	0.711
200	1.45	1.42	0.689	0.690
300	1.36	1.35	0.688	0.689
400	1.32	1.31	0.683	0.684

Source: After Nathanson [7] (With permission).

horizontal) and operating frequency [7]. Values for a and b at other frequencies can be obtained by interpolation using a logarithmic scale for a and frequency and a linear scale for b. Using these coefficients in equation (4.11) gives the expected one-way attenuation in rain as a function of rain rate for four radar frequencies, shown in Figure 4-6.

Since the magnitude of the electric field vector in circular polarization is based on the vector summation of the linear H and V field components, the circular polarization attenuation can be estimated according to

$$\alpha_{RHC} = \alpha_{LHC} = \frac{1}{\sqrt{2}}\sqrt{\alpha_{HH}^2 + \alpha_{VV}^2} \tag{4.12}$$

where α_{RHC}, α_{LHC}, α_{HH}, and α_{VV} are the attenuation coefficients for right-hand circular, left-hand circular, horizontal, and vertical polarizations. The $\sqrt{2}$ factor is used to normalize the energy in the circular wave to that of the VV or HH equivalent.

For rain rates of interest (typically less than 10 mm/hr), Figure 4-7 indicates only a slight difference between HH and VV attenuation coefficients. At higher rain rates, horizontal polarization seems to suffer slightly higher attenuation than vertical. The higher attenuation for horizontal polarization is due to a slight flattening of the falling raindrops when they become large, with the shape changing from a sphere to an oblate spheroid. With $\alpha_{VV} = k \cdot \alpha_{HH}$, $k \leq 1$, equation (4.12) becomes

$$\begin{aligned}\alpha_{RHC} = \alpha_{LHC} &= \frac{1}{\sqrt{2}}\sqrt{\alpha_{HH}^2 + k^2\alpha_{HH}^2} \\ &= \sqrt{\frac{1+k^2}{2}} \cdot \alpha_{HH}\end{aligned} \tag{4.13}$$

In rain for low rain rates there is little attenuation difference between linear and circular. As rain rate increases beyond about 10 mm/hr, the attenuation of horizontal polarization

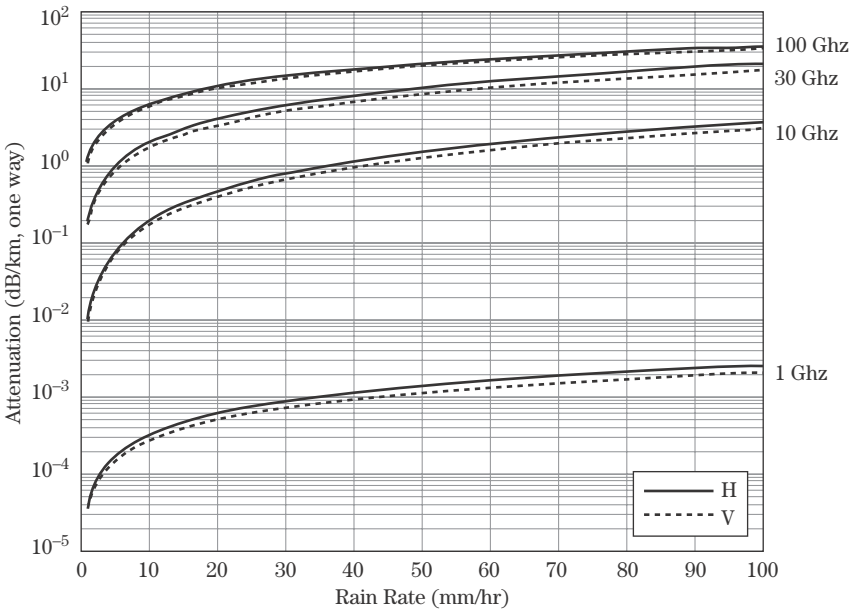

FIGURE 4-7 ■ One-way attenuation versus rain rate at four frequencies.

TABLE 4-3 ■ Summary of Fog Types and Water Concentration Ranges

Type	Water Concentrations (g/m^3)	Remarks
Steam fog	0.1–1.0	Results from cold-air movements over warm water
Warm-front fog	0.1–1.0	Evaporation of warm rain falling through cold air, usually associated with the movement of a warm front, under certain humidity, conditions yields a supersaturated air mass at ground level
Radiation fog	0–0.1	Results from radiation cooling of the earth's surface below its dew level
Coastal and inland ground fog	0.1–1.0	Radiation fog of small heights
Valley fog	0.1–1.0	Radiation fog that forms in valleys
Advection fog	0–0.1	Formed by cool air passing over a colder surface
Up-slope fog	0.1–1.0	Results from the adiabatic cooling of air up-sloping terrain

is greater than that of vertical ($k < 1$), and equation (4.13) shows that the magnitude of circular polarized energy begins to suffer measurably higher attenuation than linear magnitudes.

4.4.3 Fog

Fog is usually a result of a condensation process that occurs at or near the ground. Evaporation leads to a supersaturated condition and the formation of fog. Other occurrences of fog relate to clouds coming in contact with the ground, such as the drifting of a strata cloud into a mountain slope. Fog water content can be characterized according to Table 4-3 [3].

Fog consists of water droplets in most instances but in cold climates may be composed of ice particles. Fog formations include the presence of small drop sizes less than 100 μm in diameter. Because of the meteorological conditions associated with fog formations, the particulate size distributions may vary considerably between fog formations, even at the same or similar locations. Humidity values of 95–100% are normally associated with fog except over salt water, where values of 75–90% are common. The water concentration of fog formations is lower than that of typical water clouds, a few hundredths of a gram per cubic meter compared with values of 0.1 g/m^3 or more for clouds.

One-way attenuation (dB/km) due to fog is computed from the water concentration, M (g/m^3), frequency, f (GHz), and temperature, T (°C), according to [4,8]:

$$\alpha = M\left(-1.347 + 0.66f + \frac{11.152}{f} - 0.022T\right), \quad f > 5 \text{ GHz} \tag{4.14}$$

The fog attenuation at lower frequencies (below 5 GHz) is considered negligible for most applications. Typical values of attenuation due to fog are 0.02 to 3 dB/km at frequencies of approximately 10 GHz or higher. Higher temperatures result in higher attenuation at radar frequencies. The radar attenuation due to fog in the medium at three frequencies is illustrated in Figure 4-8.

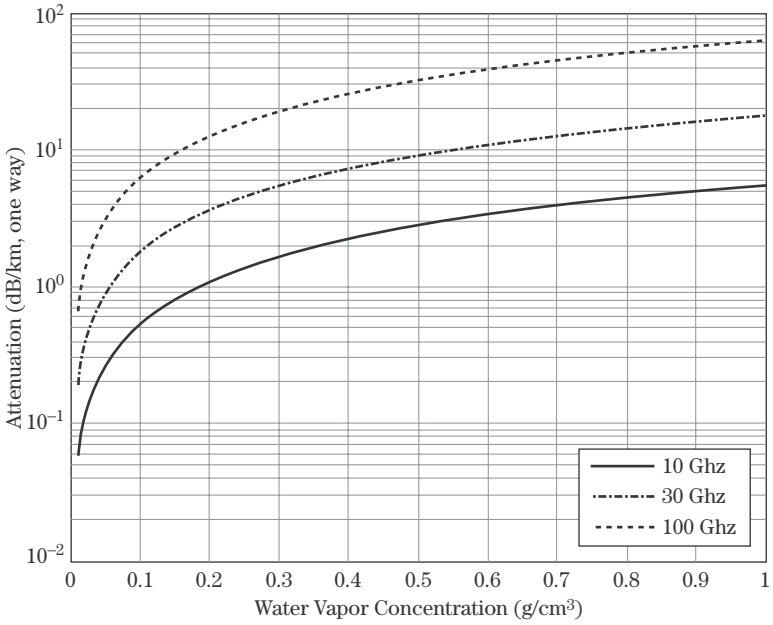

FIGURE 4-8 ■ Attenuation at three frequencies for fog versus water concentration (fog type).

4.4.4 Snow and Hail

Snow and hail differ from water particulates in two ways. The index of refraction of ice is different from that of liquid water. Snow and hail also are generally composed of aspherical, crystalline particles and are treated similarly when estimating attenuation based on equivalent fall rate. Consequently, snow and hail have very different scattering and absorption properties from rain or fog.

Table 4-4 illustrates data compiled by Nakaya and Terada [9] from their observations on Mt. Tokati, Japan, for air temperatures between $-8°$C and $-15°$C. The snow mass concentration may be converted to the equivalent rainfall rate r_e (mm/hr) according to [3]:

$$r_e = Xv \tag{4.15}$$

where X is the mass concentration of snow (g/m^3), and v is the velocity of the snowfall (m/s). The one-way attenuation α (dB/km) due to snow is then given by [3]

$$\alpha = 0.00349\frac{r_e^{1.6}}{\lambda^4} + 0.00224\frac{r_e}{\lambda} \tag{4.16}$$

The attenuation at four frequencies for snow based on data presented in Table 4-4 as a function of equivalent rain fall rate is illustrated in Figure 4-9. Several observations can be made from these data:

1. The attenuation increases with increasing fall rate, which is also true for rain.
2. Wet snow (snow containing liquid water) causes higher attenuation than dry snow for a given fall rate.
3. Attenuation generally increases with radar frequency.
4. Hail attenuation is traditionally computed in the same way as snow by defining the proper equivalent fall rate.

TABLE 4-4 ■ Mean Diameters, Masses, and Fall Velocities of Snow Crystals

Snow Type	Diameter (mm)	Mass (mg)	Fall Velocity (cm/s)
Needle	1.53	0.004	50
Plane dendrite	3.26	0.043	31
Spatial dendrite	4.15	0.146	57
Powder snow	2.15	0.064	50
Rimed crystals	2.45	0.176	100
Graupel	2.13	0.80	180

Source: From Nakaya and Terada [9] (With permission).

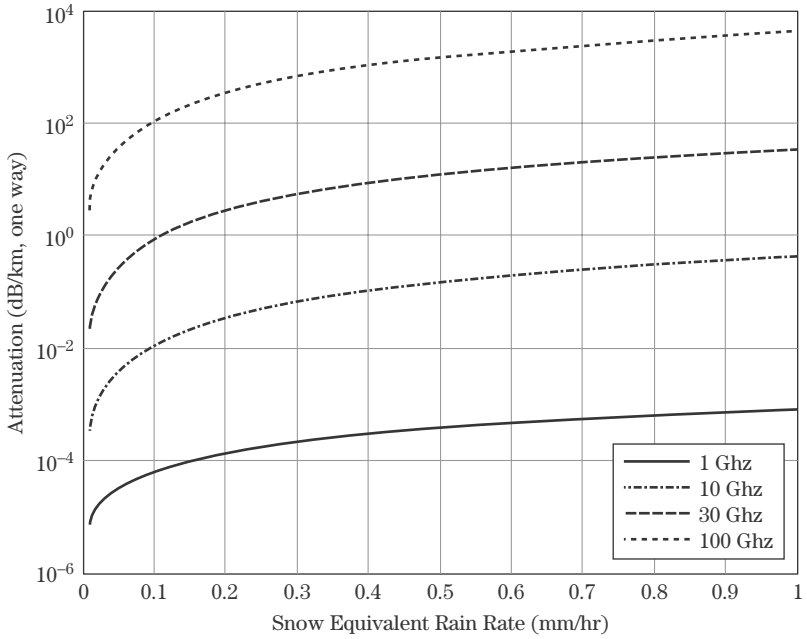

FIGURE 4-9 ■ Attenuation for snow versus equivalent rainfall rate at four frequencies.

4.4.5 Dust

For most dry soil particle concentrations in the atmosphere, the attenuation at 10 GHz is negligible (e.g., <0.0001 dB/km). This is true for dust particles up to a diameter of 300 μm. For most types of suspended particulates, the one-way attenuation α (dB/km) can be approximated as a function of *extinction efficiency,* η (m^2/g), and particulate concentration, M (g/m^3) [10,11][3]

$$\alpha = 4343 \cdot \eta M \text{ dB/km} \tag{4.17}$$

where extinction efficiency is the sum of the scattering and absorption efficiencies or the efficiency of the dust in scattering or absorbing the radar waves, respectively.

Dust particulate concentrations are generally low except in some very brief man-made instances (e.g., blowing up a dirt pile). Even the heaviest dust storm will likely have concentrations less that 0.1 g/m^3.

[3]Extinction efficiency relates to how quickly the particulates disburse when lofted and thus the reduction of attenuation through them.

4.4.6 Smoke

The smoke considered here is generally "fog oil" from a running engine. Other naturally occurring smokes can arise from burning of natural materials such as wood or rubber. For smoke, the attenuation can be expressed—similarly to dust—as a function of extinction efficiency.

Historically, smokes and obscurants have played an important role on the battlefield, and their anticipated presence on future battlefields is evidenced by the fact that some combat identification devices have requirements including operating in engine smoke. In recent years both U.S. and foreign countermeasure developers have extended their smoke developments to include radar bands. Indeed, the U.S. Army has classified the M-81 grenade for armor self-protection because it produces a cloud that is an effective obscurant in visible, infrared (IR), and MMW regions of the spectrum.

Unlike dust, fog, rain, and even fog oil, aerosols are specifically designed to affect specific wavelengths. Whereas the extinction efficiency of 4 mm/hr rain at 10 GHz is on the order of 10^{-3} m^2/gm, the extinction efficiency of average X-band aerosols is approximately 1.0 m^2/gm. Thus, it requires far less aerosol material to cause a significant attenuation effect. Recent advances in aerosol development have focused on developing multispectral aerosols that introduce attenuation in radar-, infrared-, and laser-operating bands simultaneously.

4.5 ATMOSPHERIC REFRACTION

Refraction is the change in the direction of travel of radio waves due to a spatial change in the index of refraction. The index of refraction n is equal to

$$n = \frac{c}{v_p} \tag{4.18}$$

where c is the speed of light in a vacuum (well approximated as 3×10^8 m/s), and v_p is the phase velocity of the wave (m/s) in the medium. The index of refraction is unitless. It is measured based on standard meteorological observations of air temperature, atmospheric pressure, and partial pressure of water vapor. Averaged over many locations and long periods of time, the index of refraction of the troposphere generally decreases with increasing altitude.

The refractive index variation present in the troposphere can significantly affect the propagation of radio waves. The results of these variations are divided into *standard* and *anomalous* atmosphere effects. Standard refraction implies that the relationship between refractive index and height is approximately linear: the effective Earth radar horizon model. Propagation conditions that deviate from this linear model are called *anomalous* but are not necessarily infrequent. Anomalous atmosphere conditions are in turn divided into three subcategories: *subrefraction*, *superrefraction*, and *trapping* or *ducting*.

For standard atmospheres, the net effect of refraction is a bending of a horizontally transmitted radio wave toward the earth's surface, which can cause increased errors in range and angular position measurements but also can allow propagation into masked or shadow zones. Figure 4-10 illustrates the general effect of each of these phenomena on a ray trace from a transmitter.

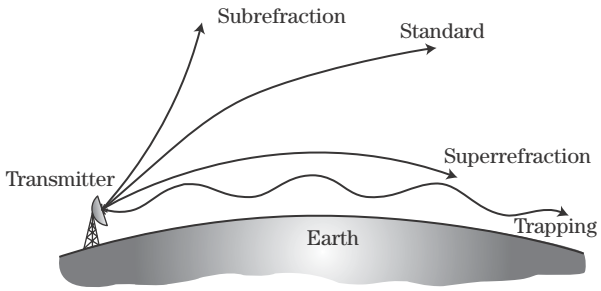

FIGURE 4-10 ■ Illustration of ray bending for standard and anomalous refraction profiles.

4.5.1 Standard Refraction

4.5.1.1 The Standard Atmosphere

For wave propagation in clear air the *standard atmosphere*, which also implies standard refraction, is most often used to describe the conditions of the medium. The standard atmosphere is actually a series of models that define the values for atmospheric temperature, pressure, and density as well as other parameters, such as sound speed, viscosity, and thermal conductivity. These parameters are presented in tables as a function of altitude, with varying resolutions ranging from 0.05 km at low altitudes to 5 km at higher altitudes. The most commonly referenced model is the U.S. Standard Atmosphere [12], but the reader should be aware that other models are available, such as the Standard Atmosphere of the International Civil Aviation Organization [13] and the International Standard Atmosphere [14]. Each model has various refinements, although most of them differ only in the region above approximately 30 km. Because of this, the U.S. Standard Atmosphere is suitable for most calculations below that altitude.

The path of a ray traveling through the atmosphere can be determined from Snell's law. For a first approximation, the earth's surface can be modeled as a plane, with the atmosphere modeled as a series of planar slabs above it, each having a constant index of refraction (see Figure 4-11). From Snell's law, one obtains

$$n_0 \cos\alpha_0 = n_1 \cos\alpha_1 = n_2 \cos\alpha_2 \ldots = n_i \cos\alpha_i \tag{4.19}$$

where n_i is the index of refraction of the i-th slab. Thus, if n_0 and the angle α_0 at which the wave is transmitted are known, the subsequent angles α_i can be found from Snell's law at each of the layer boundaries, and the path of the ray can be determined as it travels through the layers.

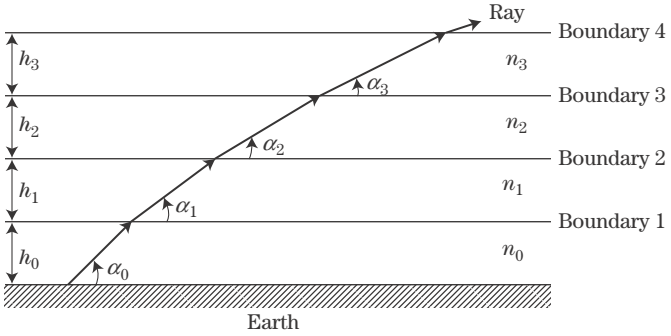

FIGURE 4-11 ■ Path of a ray through a horizontally stratified atmosphere (troposphere).

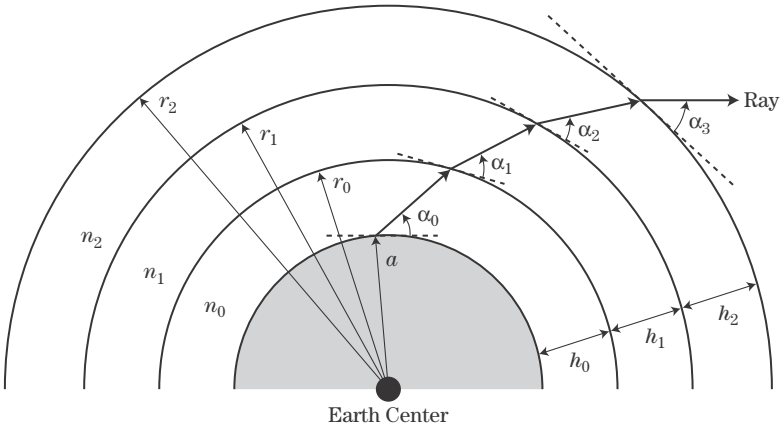

FIGURE 4-12 ■ Path of a ray through a radially stratified atmosphere (troposphere).

A more accurate solution to the refraction problem is obtained by assuming that the earth is spherical instead of planar and that the electrical properties of the atmosphere are constant between concentric spheres of outer radii, r_i (see Figure 4-12). For such a radially stratified medium, Snell's law assumes the form

$$n_0 r_0 \cos\alpha_0 = n_1 r_1 \cos\alpha_1 = n_2 r_2 \cos\alpha_2 \ldots = n_i r_i \cos\alpha_i \tag{4.20}$$

Both the planar and spherical approximations improve as the thickness of each slab is made smaller.

The curved path traveled by an EM wave due to refraction causes errors in the estimate of target location in both range and angle. This effect is illustrated in Figure 4-13. In the standard refraction case, the waves travel along the curved path bending slightly downward toward the earth at each layer. The effect is to yield measured ranges and elevation angles that are larger than the true values.

The resulting elevation angle and range errors for a spherically stratified model and standard atmosphere are shown in Figures 4-14 and 4-15. In these figures, the altitude is that of the radar system. According to Berkowitz [15], angle errors can range from approximately 0.1 to 0.8 degrees and range errors from 10 to 381 feet, depending on relative humidity and transmitter height in a standard atmosphere. These errors impact the

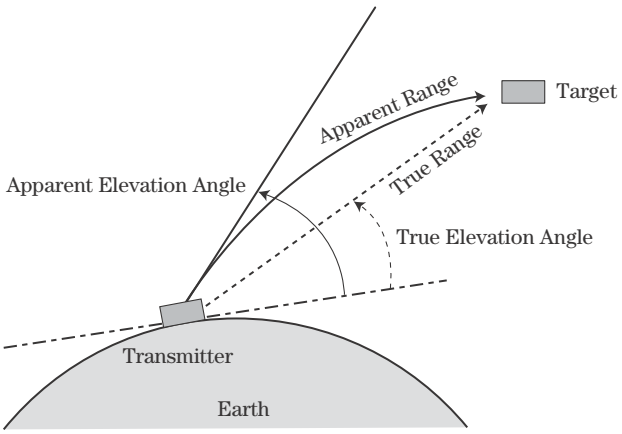

FIGURE 4-13 ■ Normal refraction effects on target location (troposphere).

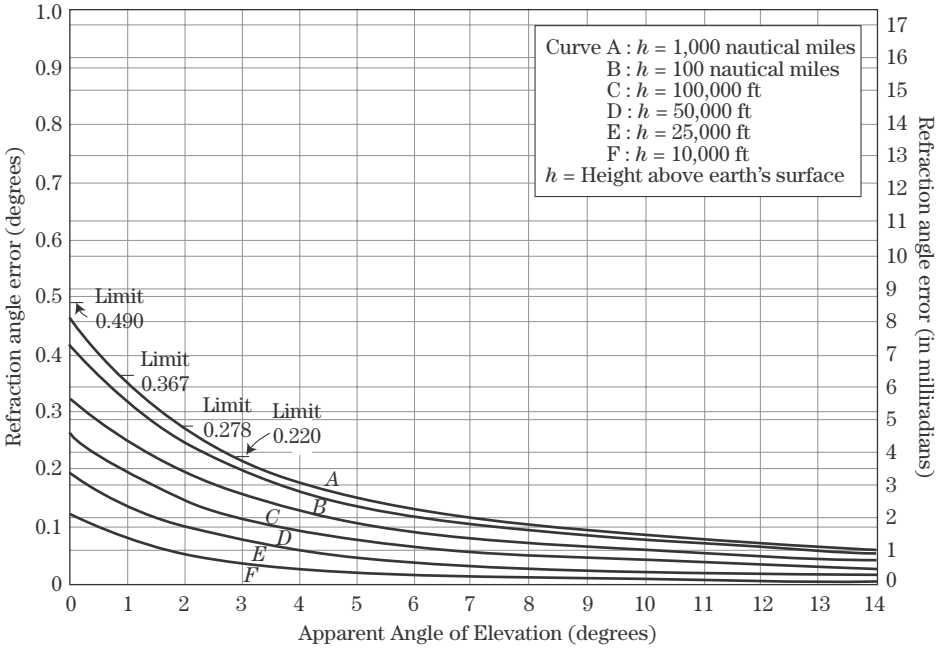

FIGURE 4-14 ■ Normal refraction effects on target location—angle estimate, 0% humidity (troposphere).

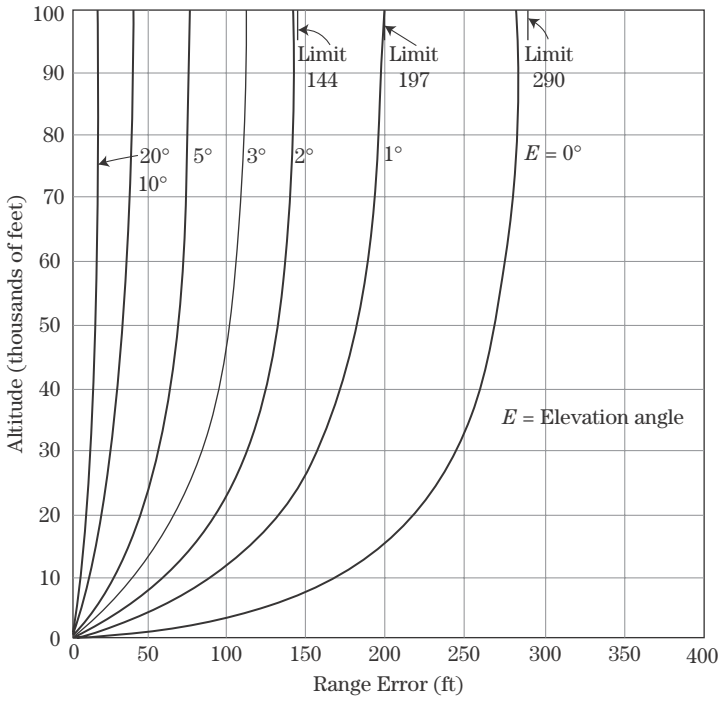

FIGURE 4-15 ■ Normal refraction effects on target location—range estimate, 0% humidity (troposphere).

ability of the radar to achieve angle error requirements and intercept receivers to achieve positional estimates. In most cases the refraction effects are significant for longer-range applications. For example, an elevation error of only 5 milliradians (approximately 0.3 degrees) at 1,000 kilometers is equivalent to a target position error normal to the radar boresight of over 5 kilometers.

While the relationships presented here are good first-order approximations, the atmosphere is not so easily stratified. The index of refraction versus height curve varies for different points on the earth. Bean and Dutton [16] compiled information about the index of retraction as a function of height for various locations on the earth's surface that can be used to refine the estimate of refraction impacts.

4.5.1.2 Defining the Horizon: The Effective Earth Model

One effect of refraction of EM waves is the extension of the apparent horizon over the "spherical" earth for ground-based radars close to the earth. The concept of an *effective Earth radius* is an alternative way to account for the effects of a standard atmosphere and in particular to predict the additional range associated with the refractive horizon for a transmitter. It is important to keep in mind that for space-based or airborne radars or for ground radars looking significantly above the horizon, these results are not as pronounced.

The radar horizon on the "spherical" earth can be shown to be

$$R_h = \sqrt{2ah_t} \tag{4.21}$$

where a is the earth's radius (m), and h_t (m) is the height of the transmitter (or receiver) above the earth's surface. The extended horizon, R_h', due to refraction can also be predicted using equation (4.21) if an *effective Earth model* having a slightly larger radius a_e is used. This idea is illustrated in Figure 4-16.

For standard atmospheres (typical refractive index gradient $dn/dh = 3.9 \times 10^{-8}$ m) and the actual earth radius a of 6370 km, the ratio between the actual and effective radius can be shown to be approximately 4/3 [2,17]. This is the origin of the "4/3 Earth radius" or *4/3 Earth* model cited in many texts for radar horizon computations over land. From equation (4.21), the increase in radar horizon is then $\sqrt{4/3}$, or about 15%, making $a_e = (4/3)a$. Figure 4-17 illustrates the increase in the radar horizon based on ray bending in standard refraction as a function of transmitter height.

4.5.2 Anomalous Refraction

Standard refraction implies that the relationship between refractive index and height is linear. Propagation conditions that deviate from this linear model are called *anomalous*,

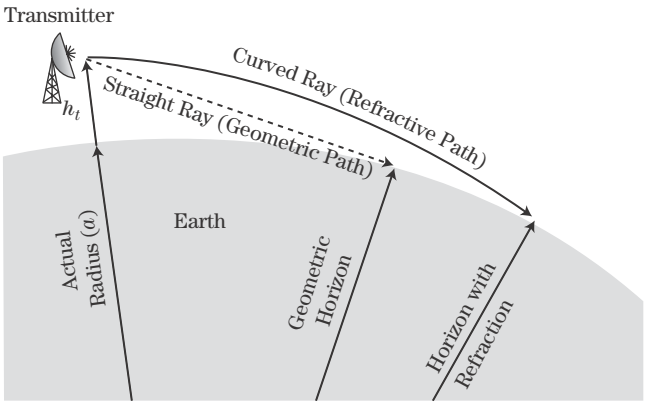

FIGURE 4-16 ■ Increased range to radar horizon due to refraction.

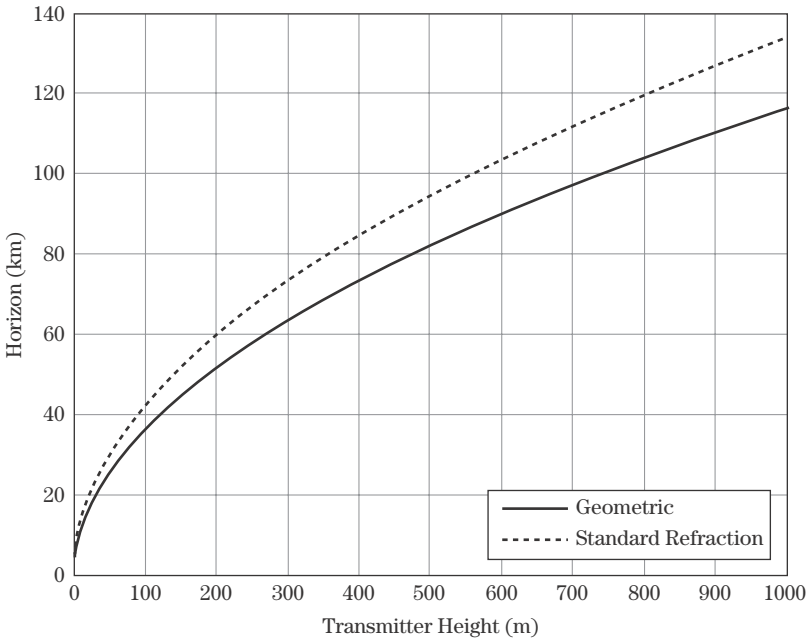

FIGURE 4-17 ■ Comparison of radar horizons in free space and a standard atmosphere.

though they are not necessarily infrequent. Three forms of anomalous deviation are possible:

1. *Subrefraction* occurs when the rate of change of the refractive index, *n,* as a function of altitude, *h,* is positive or zero ($dn/dh \geq 0$). This condition bends rays upward, thus decreasing the ground coverage of a radar.
2. *Superrefraction* occurs when *dn/dh* is more negative than in a standard atmosphere. This condition causes waves to bend more strongly toward the ground and can increase the range of the radar at low elevations (angles less than 1.5 degrees) but has little effect on high-angle coverage.
3. *Ducting and trapping* occurs when $dn/dh < -16 \times 10^{-8}\ \text{m}^{-1}$. Under this condition, the radius of curvature of the ray is less than or equal to the radius of curvature of the earth, trapping transmitted energy in a "parallel plate waveguide" near the earth. A duct can be formed when the temperature increases with height near the surface (temperature inversion) or the humidity decreases (moisture lapse) with height. These ducts can dramatically impair or enhance radar coverage and range depending on whether each link terminal in the radar/target or radar/receiver pair are located in or out of the ducts. Most of these effects are seen at very high frequency (VHF) and ultra high frequency (UHF). Note that in some texts a distinction is made between trapping and ducting, because trapping is a result of the same processes that cause superrefraction, as is ducting. However, in the case of trapping, the energy remains between the atmospheric boundary and the earth, creating an atmospheric waveguide.

Of these effects, ducting is the most important for radar. Ducting and trapping redistribute the radar beam over an elevation search area, causing gaps in coverage as illustrated in Figure 4-18 for ground-based radar. Under airborne radar conditions, much of the transmitted energy is redistributed into a low-elevation surface duct, significantly enhancing

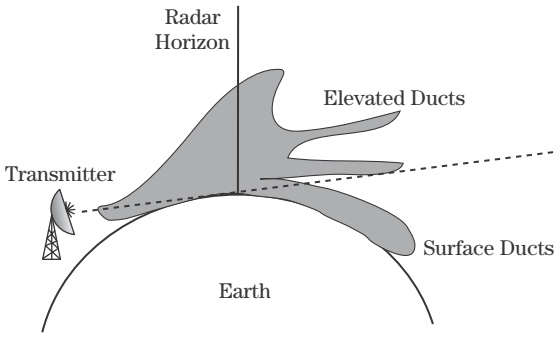

FIGURE 4-18 ■ Illustration of energy propagation over the radar horizon and gaps in coverage due to ducts.

ground coverage and range at low elevations while introducing shadow zones above the duct, as illustrated in Figure 4-19. This energy redistribution causes the performance above and inside the duct to degrade, reducing the radar's range performance for target, clutter, and weather detection.

In Figure 4-19 the incident wave is both reflected from and transmitted into the duct at point *A*. The transmitted energy in the duct reflects off the surface at point *B* back toward the top of the duct. Once at the top of the duct some of this energy transmits through the boundary and interferes with the reflected wave from *A* causing shadow zones. As the trapped energy in the duct continues to bounce around, the waves form additional interference patterns and shadow zones inside as well. In addition, for some airborne systems increased ground coverage can compromise the ability of the system to perform covert missions.

Atmospheric ducts are generally on the order of 10 to 20 meters in height, never more than about 200 meters. One type, the *evaporation duct*, is found regularly over relatively warm bodies of water. It is caused by a temperature inversion near the surface and is accentuated by the intense relative humidity near the surface due to water evaporation. These conditions can correspond to high temperatures ($>70^{\circ}$F) and relative humidity above 75% [18]. Over land surfaces an evaporation duct is formed when an intense layer of low-lying humidity is found over a surface that is cooling more rapidly than the surrounding air (e.g., fog conditions). This condition is also representative of conditions when a large daytime temperature inversion over a locally cool surface caused by intense air temperature from heat reradiated from surrounding surfaces (e.g., over gray concrete runway surrounded

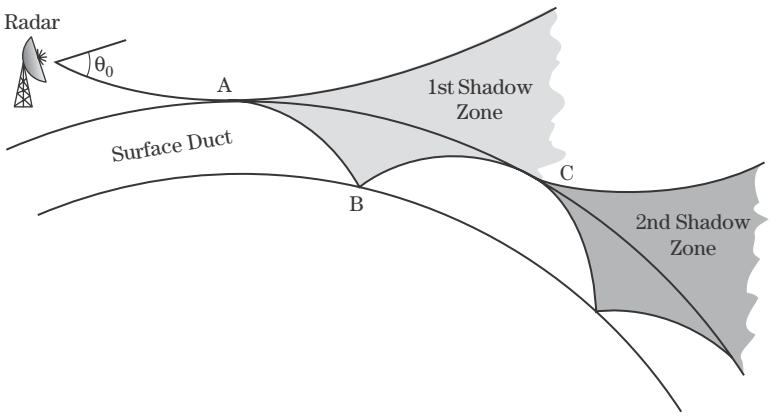

FIGURE 4-19 ■ Illustration of energy redistribution and loss in coverage when transmitter is above a surface duct.

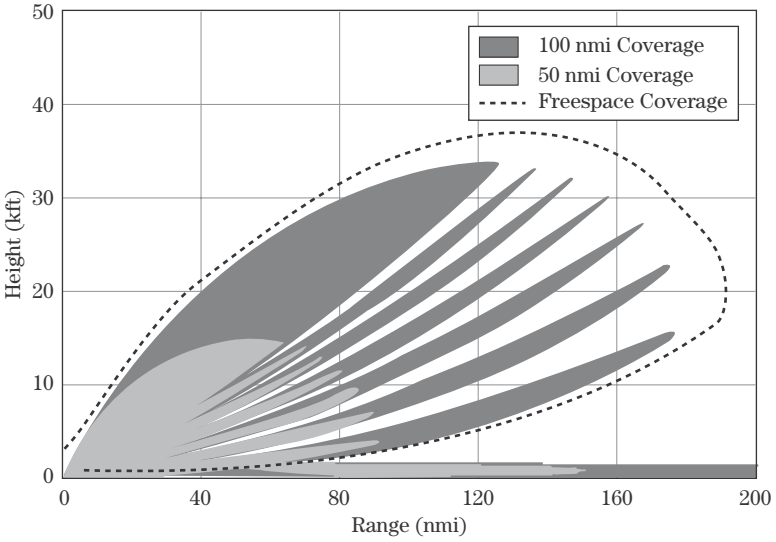

FIGURE 4-20 ■ Illustration of ducting loss in radar elevation coverage.

by black asphalt). The potential for both evaporation and elevated ducts exists in coastal regions where there are large temperature contrasts between land and water. These land–water temperature differences and their diurnal reversal produce corresponding land–water air pressure differences, resulting in a system of breezes across the shoreline that reverses its direction between day and night.

The net effect of these ducts is a redistribution of transmitted energy. The presence of extended ranges at some elevations comes at the expense of reduced ranges or radio "holes" at other elevations. Although precise elevation profiles for ducting propagation factor are not easily computed analytically, a good rule of thumb for propagation inside of a duct is to assume the one-way power falls off according to R^{-1} instead of R^{-2} [19,20]. The trapped rays may also coherently combine, causing potentially large signal fading due to the interference between the several modes.

In general, a computer model that includes an atmospheric profile is required to determine the propagation factor as a function of elevation for a particular scenario. Figure 4-20 is an example of the EREPS simulation [21] results for radar coverage based on a 3.3 GHz wave launched above an inhomogeneous evaporation duct. A list of some useful off-the-shelf simulations to determine these profiles and other propagation mechanisms are provided at the end of this chapter.

4.6 TURBULENCE

Most people have seen the phenomenon of a blurry area appearing above a hot asphalt road. This effect is essentially a turbulence phenomenon at the eye's (optical) wavelength. The same turbulence-induced fluctuations of refractive indexes in the path through the atmospheric media can impact very short wavelength radar.[4] Atmospheric turbulence effects are generally considered to be a high-frequency phenomenon and as such are likely

[4]Typically at millimeter wavelengths or smaller.

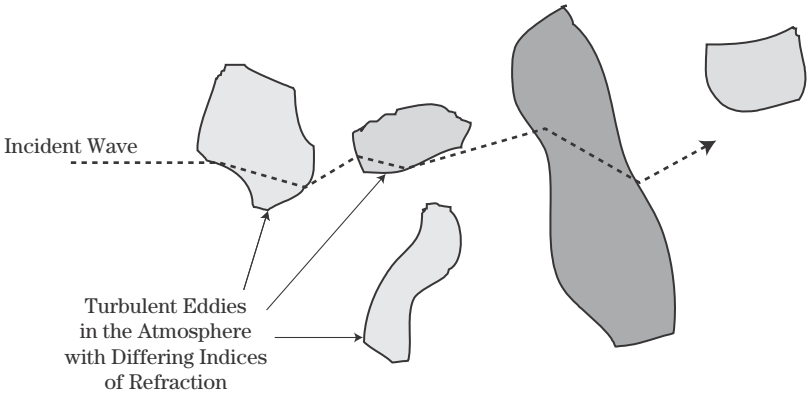

FIGURE 4-21 ■ Illustration of turbulence "pockets" in atmosphere.

significant only at frequencies of 80 GHz or higher. The worst case for atmospheric fluctuations occurs in clear, hot, humid weather and not in rain or snow as might be expected. The smallest fluctuations in both amplitude and phase tend to occur during a dense fog [22].

Radiofrequency (RF) energy is subject to phase and amplitude *scintillation* in atmospheric media, which exhibit point-to-point refractive index variations caused by small fluctuations in temperature and humidity. Intensity fluctuations probably are too small to be of consequence even at millimeter waves. Depolarization, frequency shift, and thermal blooming are other turbulence effects that can sometimes be observed at optical wavelengths but whose effects are likely negligible at RF [18].

Perhaps the major potential problem caused by atmospheric turbulence is angle of arrival (AOA) fluctuations, which are related to phase shifts by the relation $\theta = \phi/kd$, where θ is AOA, ϕ is phase shift, $k = 2\pi/\lambda$ is the wave number, and d is the separation between points in the wavefront. Index of refraction variations induce phase shifts across the wavefront of a propagating signal. These in turn can give rise to changes in the apparent angle at which the wavefront is incident on the receiver (Figure 4-21). AOA fluctuations cause a potential target to be detected at an angle different from its actual angle and thus can bring about aimpoint wander and decreased accuracy in tracking systems.

For MMW systems, amplitude fluctuations are about 1–2 dB and AOA fluctuations are about 300 microradians peak under worst-case conditions. In one experiment, 94 GHz data collected over a fairly short range path indicated that the total fluctuation in angle of arrival due to atmospheric turbulence was about 0.56 milliradians [23].

4.7 EXPLOITING THE IONOSPHERE

The ionosphere is a region of the upper atmosphere (thermosphere) that contains a sufficient number of ionized particles to affect radio propagation. The ionization of the atmospheric gases is produced primarily by the ultraviolet light from the sun. It increases with height, though not linearly, and tends to have maxima at certain heights defining layers. The shaded areas in Figure 4-22 illustrate the four main regions of high ionization.

The characteristics of the four main ionosphere layers are as follows:

1. The *D layer* exists only during daylight hours, at which time it bends and absorbs low frequency (f < 3–7 MHz) waves.

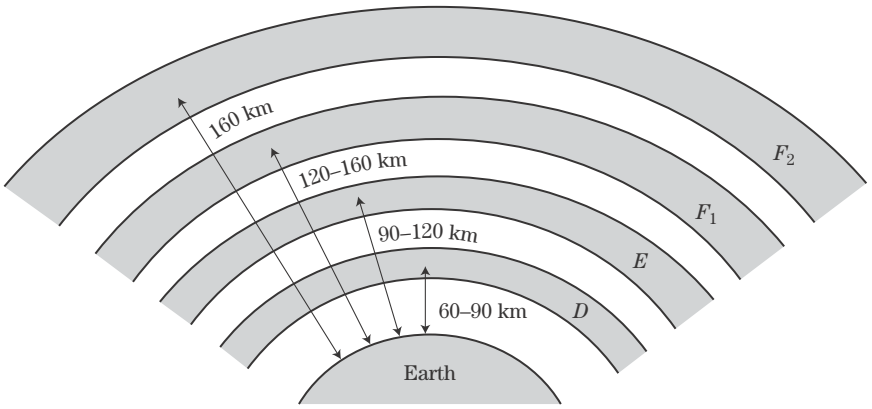

FIGURE 4-22 ■ Layers of the ionosphere (typical of noontime locations).

2. The *E layer* has characteristics similar to those of the D layer but exists at greater heights in the atmosphere.
3. The *F1 layer* is weaker and less influential on radar waves than the F_2 layer.
4. The *F2 layer* is the most important layer for long-distance transmission. It bends waves at frequencies below 30–50 MHz. Its influence is strongest during the daytime and decreases somewhat at night, when it tends to combine with the F1 layer.

The afternoon behavior of ionized layers retraces the morning values relative to local noon, providing a higher level of behavioral consistency.

The ionosphere is a dispersive medium in which the phase velocity of the waves is greater than c, resulting in a refractive index of less than 1.0. This causes rays passing into a region of increasing electron density to be bent away from the normal and back toward the ground. The bending effect of a region on EM waves can be described by Snell's law and the refractive index, n, of the layer region, as described earlier. For the ionosphere the refractive index, n, is computed from [2]

$$n = \sqrt{1 - \left(\frac{f_p}{f}\right)^2} \tag{4.22}$$

where f is the transmit frequency (Hz), and f_p is the plasma frequency for the layer based on its electron density, N_e (electrons/m^3).

$$f_p \approx 9\sqrt{N_e} \tag{4.23}$$

Typical electron density of the F2 layer during the day (noontime) ranges from 10^{11} to 10^{12} electrons/m^3.

The effect of one ionized layer on several rays is shown in Figure 4-23. A ray penetrates farther into the layer as the angle the ray makes with the horizon is increased. Rays

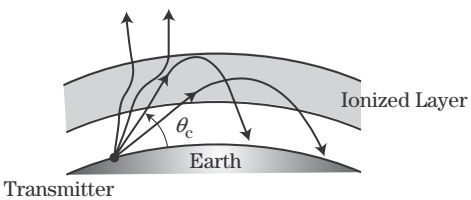

FIGURE 4-23 ■ Bending of rays passing through an ionized layer at difference incidence angles.

transmitted at angles greater than the critical angle do not return to Earth.[5] The ionosphere is therefore most influential at low angles of incidence and for low frequencies. The maximum "extended" distance that can be covered by a single reflection hop is about l,250 miles for reflection from the E layer and 2,500 miles for reflection from the F2 layer. OTH radars use this fact and exploit one or more hops to obtain radar coverage at regions that are thousands of miles away and that are impossible to cover from such distances with microwave or higher-frequency radars.

As Figure 4-23 shows, rays launched at an angle greater than the critical angle are still affected by the ionosphere as they pass through it. Thus, space-based radars (or ground-based radars tracking objects in space) must take such effects into account when calculating, for example, ranges, range rates, and Doppler shifts. Depending on the operating frequency of the radar system, various effects must be considered. For instance, at 435 MHz one can expect approximately 1.5 complete rotations of the phase vector of the wavefront of the radar beam due to Faraday rotation. This effect diminishes as the frequency increases, so that at 1.2 GHz less than a quarter of a rotation in phase occurs.

4.8 DIFFRACTION

Diffraction is a mechanism by which waves can curve around edges and penetrate the shadow region behind an opaque obstacle. This effect can be explained by Huygens's principle, originally introduced in Chapter 1, which states that every elementary area of a wavefront can be considered a source that radiates isotropically on its front side. The new waves will interfere with each other in the shadow zone to produce an interference pattern at the observation point as illustrated in Figure 4-24.

As the incident wave diffracts around the obstacle it will recombine with scaled replicas of itself within the observation plane. The interface pattern produced is that of two new waves originating from virtual phase centers at *P*. These virtual phase centers are also known as *virtual sources* and are an equivalent representation of the incident wave structure *after* diffraction has occurred.

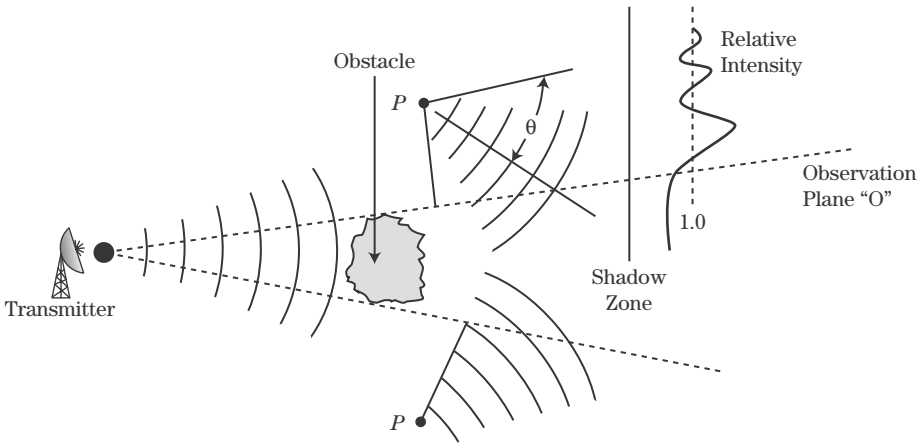

FIGURE 4-24 ■ Illustration of virtual sources for diffraction around an obstacle.

[5]Note that a signal will be totally reflected by the ionosphere if its frequency is less than the ionized layer's plasma frequency independent of incidence angle.

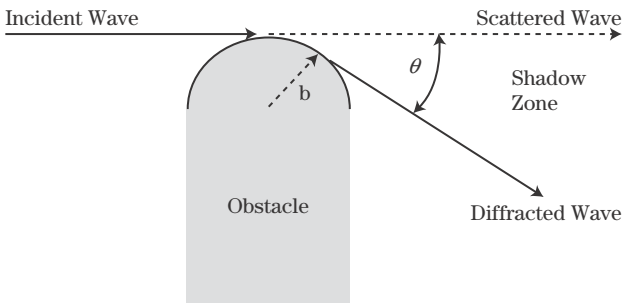

FIGURE 4-25 ■ Geometry for diffraction into shadow zones.

Depending on the transmitted wavelength, the edges of the diffracting object may be appear as a smooth, curved edge or as a sharp *knife edge* or wedge. At the boundary between the interference and diffraction regions, some signal enhancement may be realized. In general, as the observation angle falls into the shadow zones, diffracted wave attenuations increase.

The electromagnetic field in the shadow zone due to diffraction can be represented by an infinite series of terms called *modes* [24]. The effect of diffraction on the signal strength in or near the shadow region can be represented using a one-way power propagation factor, F^2, in this case called the *diffraction coefficient*.

The behavior of the diffraction coefficient is modeled by considering diffraction around a curved edge of radius b as shown in Figure 4-25. As b goes to zero, the shape becomes a knife edge. The diffraction coefficient is a function of both the edge radius times the wavenumber k and the angle, θ, into the shadow zone, $F^2(\theta, kb)$. At or near the shadow boundary, many modes must be summed to compute the diffraction coefficient and resulting signal strength. However, in the shadow zones, the first mode is often sufficient to model knife-edge diffraction.

The knife edge is considered the most frequently occurring diffraction mechanism when a wave is impeded by an obstacle. The propagation factor, F^2, into the shadow zone for knife-edge diffraction falls off with range according to $1/kR$. The falloff as a function of shadow angle is given by Sommerfield [25] as

$$F^2(\theta, kb = 0) = \frac{1}{2\sqrt{2\pi}}\left[\sec\frac{1}{2}(\theta + \pi) + \csc\frac{1}{2}(\theta + \pi)\right] \tag{4.24}$$

For other values of b greater than about $\lambda/50$, a more general form for the amplitude roll-off into the shadow region is approximated for a Fermat surface by Keller [26,27] as

$$F^2(\theta, kb) = (kb)^{1/3}\frac{C_0}{\sqrt{2}}\exp[-\tau_0(kb)^{\theta/3}]\sin(\pi/3)\sqrt{1/k} \tag{4.25}$$

where for a real dielectric surface the appropriate mode coefficients are given in [23] as $C_0 = 0.910719$ and $\tau_0 = 1.8557\exp(\pi/3)$. Note that as the frequency of the incident field increases relative to the radii of curvature (increasing kb), there is less penetration into the shadow region (decreasing F^2). Figure 4-26 illustrates the differences in the scattered signal amplitude and angle distribution for the knife and rounded-tip edges. Figure 4-27 shows, for the two edge types, the diffracted field intensity into the shadow zone as a function of shadow angle, θ. Note the near independence with respect to shadow angle for the knife-edge case. The signal falloff for the rounded-tip case in the shadow zone is significantly greater than its knife-edge counterpart.

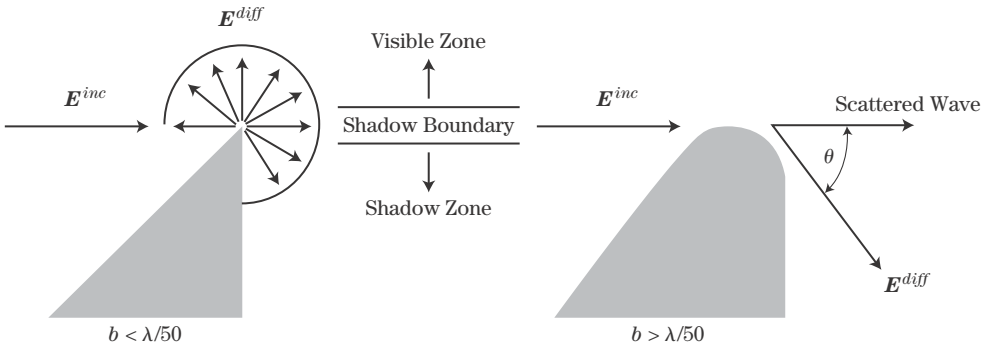

FIGURE 4-26 ■ Local diffraction coefficient, F^2, behavior for two types of edges.

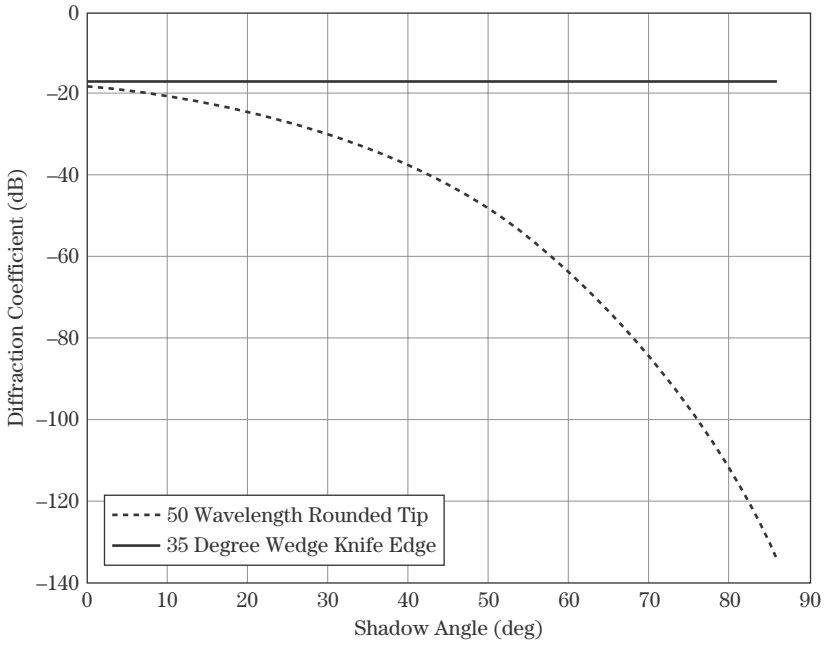

FIGURE 4-27 ■ Diffraction coefficient for rounded tip and knife edge versus shadow angle at 1 GHz.

4.9 MULTIPATH

The IEEE radar definition of multipath is "the propagation of a wave from one point to another by more than one path" [28]. When multipath occurs in radar, it usually consists of a direct path wave combined with other indirect path waves at an observation point. The signal fading (or enhancing) is a consequence of the indirect wave relative phases combining with the direct wave to produce constructive or destructive interference. Virtually everyone has experienced multipath effects on modern equipment, if not with radars. For radio and many cellular phones, sudden losses of reception in certain regions of the city may be the direct result of multipath.

Multipath wave combinations can produce complex propagation factor profiles and are highly sensitive to frequency, antenna patterns, sensor heights, and surface electrical and physical properties. Surface properties can include mountains, buildings, sand dunes,

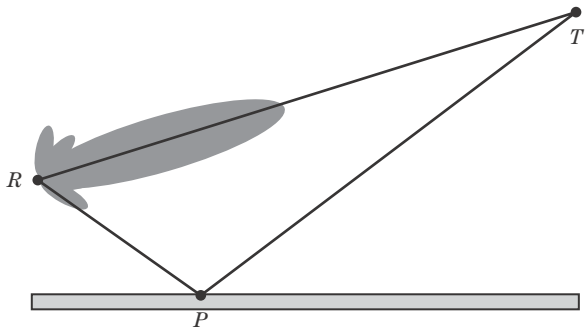

FIGURE 4-28 ■ Illustration of multipath geometry for ground reflection.

tall grass, and discrete scatters. At frequencies below about 40 MHz the multipath field at the observer may also include contributions from reflection off the ionosphere.

This section focuses on the simple case where the intermediate terrain is perfectly flat. The flat-terrain case provides the foundation for extrapolating multipath principles to more complex intermediate surfaces.

4.9.1 Propagation Paths and Superposition

When considering propagation paths it is useful to begin by defining a simple geometry. For a monostatic radar the presence of a flat ground plane adds three new two-way multipath fields. Figure 4-28 depicts a radar (R) tracking a target (T) above a ground plane (P).

The electric field amplitudes of the direct–direct (free-space) path wave and the three new field path waves are as follows:

1. E_{dd}: Path RTR (direct–direct, or DD).
2. E_{di}: Path RTPR (direct–indirect, or DI).
3. E_{id}: Path RPTR (indirect–direct, or ID).
4. E_{ii}: Path RPTPR (indirect–indirect, or II).

For the bistatic or one-way observer geometry (observer at point T), the geometry indicates that only one new path is present. E_d represents the direct field path to the receiver. The bistatic paths and vectors are as follows:

1. E_d: Path RT (D).
2. E_i: Path RPT (I).

The indirect fields will have different characteristics from the direct path due to reflection off a boundary and the additional path length they must travel to the observer. The additional path length is often denoted δR. The effect of the indirect–indirect path is commonly modeled with a virtual target, T', that exists below the ground plane. The virtual target—for analysis purposes—is at an equal distance below the plane as the real target (or observer) is above it. Figure 4-29 illustrates this concept for an air-to-ground geometry.

Neglecting the small impact on amplitude due to additional path length at the target (or observer), the indirect signal's amplitude is modified solely by the *reflection coefficient,* Γ, at reflection point P. With this in mind, the one-way power propagation factor describing the coherent sum of the direct and indirect path signals at Γ will be

$$F^2 = |1 + \Gamma \cos(k\delta R)|^2 \tag{4.26}$$

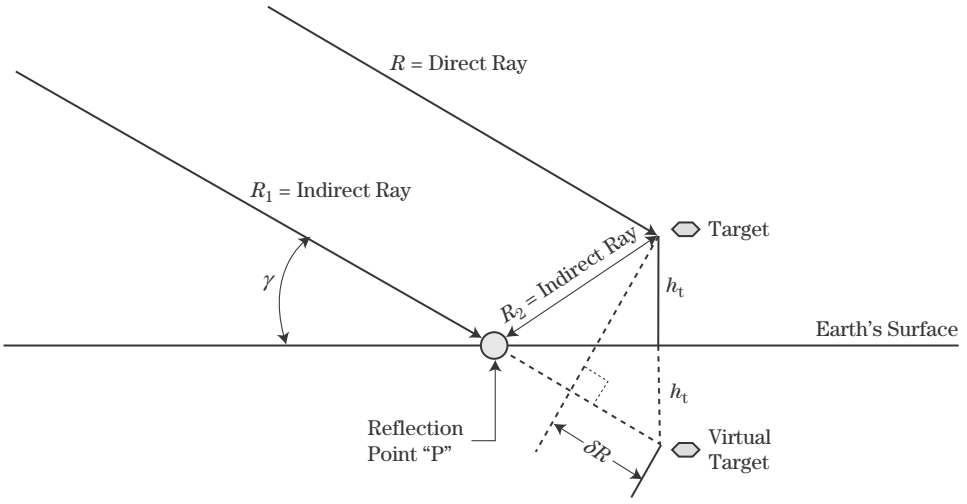

FIGURE 4-29 ■ Simplified multipath geometry for flat Earth and the virtual target.

where 1 represents the direct-path E-field magnitude, Γ is the complex reflection coefficient of the surface, k is the wavenumber, and ΔR is the difference in range between the direct path and the reflected path. For two-way geometries (e.g., radar to target and back), this factor becomes

$$F^4 = |1 + 2\Gamma \cos(k\delta R) + [\Gamma \cos(k\delta R)]^2|^2 \tag{4.27}$$

For a reflection coefficient of 1, the maximum value of F^2 (i.e., the maximum signal power enhancement due to multipath) is 6 dB (4×) for the one-way case and 12 dB (16×) for the two-way case (F^4).

For most long-range, point-to-point situations where the grazing angle, γ, is below about 5 degrees, δR may be approximated by

$$\delta R = 2h_a h_t / d \tag{4.28}$$

where $h_a$and h_t are the transmitter and target heights, respectively, and d is the ground range between them. The specular grazing angle, γ_s, defined by the simplest form of Snell's law[6] can be approximated by

$$\gamma_s = \tan^{-1}\left(\frac{h_a + h_t}{d}\right) \tag{4.29}$$

Superposition is used to determine the effect of different ray contributions to the total field. In the simplest case, the direct ray, E_d, and the forward scattered indirect ray, E_i (one-way geometry), interfere at an observation point (receiver). The composite field at any receiver in a multipath environment is the sum of the direct ray and the indirect or reflected rays (Figure 4-30), which produce significant amplitude lobing structures at the observer. The interference structure can also be classified by its lobing periodicities. The higher the frequency, the more rapidly the relative phase will change and thus the shorter the period between interference lobes. Very smooth surfaces are classified by low-frequency

[6]When the reflection is in the same medium ($n_1 = n_2$), the angle of reflection equals the angle of incidence.

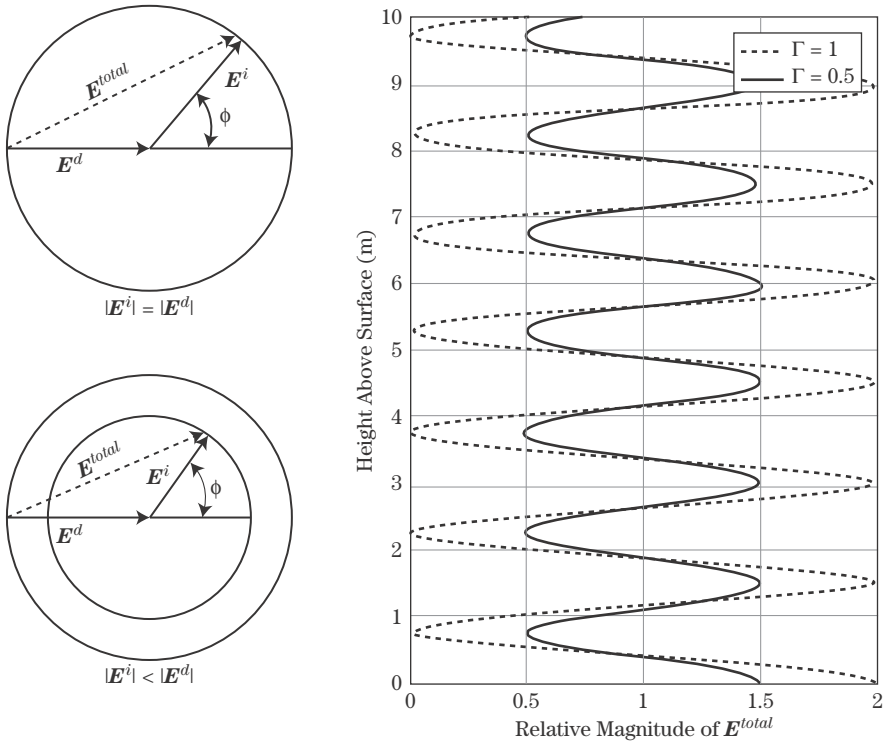

FIGURE 4-30 ■ Coherent summation of direct and indirect ray interference pattern versus observer height above ground plane (10 GHz, $h_a = 1$ m, $d = 100$ m).

components compared with rough surfaces, which have higher-frequency structures of the interference patterns lobing structure.

Figures 4-31 and 4-32 illustrate the lobing structure for the received signal as a function of range from a receiver or target in the presence of multipath. At some ranges the signal is enhanced over the free-space estimate due to constructive interference of the direct and multipath rays, allowing for extended range performance of a particular radar.

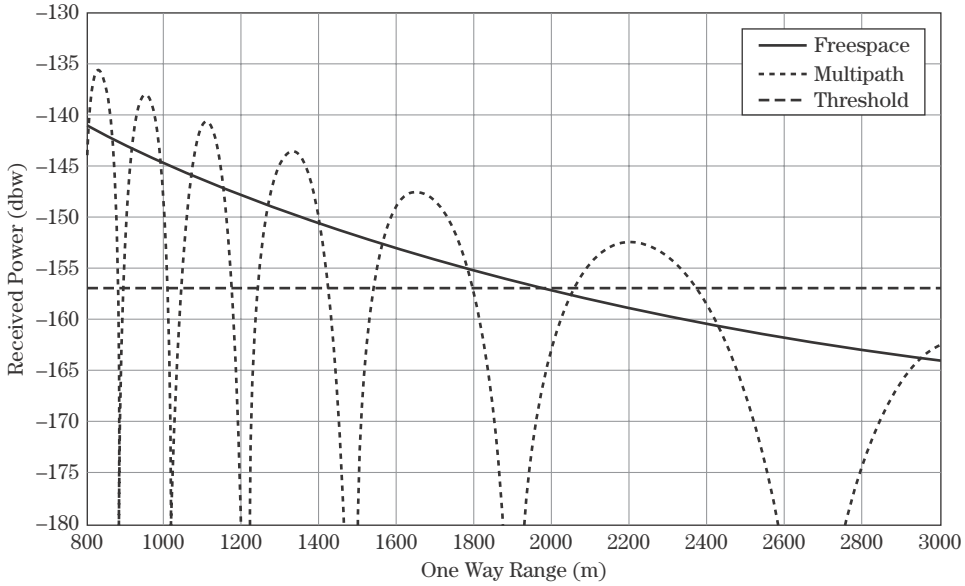

FIGURE 4-31 ■ Multipath signal lobing versus free space for one-way geometry and $\Gamma = 1$.

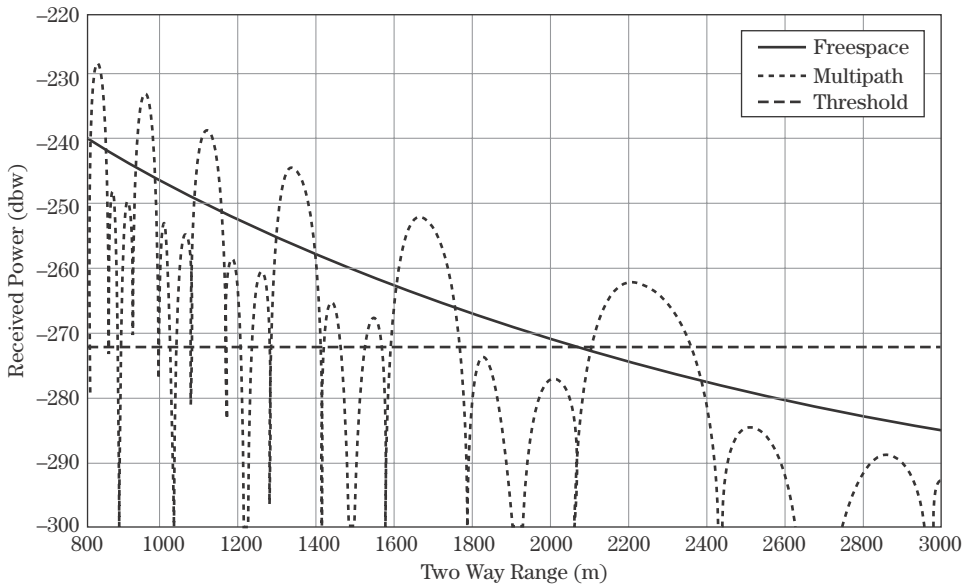

FIGURE 4-32 ■ Multipath signal lobing versus free space for two-way geometry and $\Gamma = 1$.

In the figures, note that a performance threshold is indicated for this particular radar parameter set. In both illustrations (provided for a transmitter and receiver height of 10 meters and a transmit frequency of 10 GHz), the multipath "gain" over free space actually extends the maximum range of the system's performance, by almost 300 meters in the two-way case. This gain comes at the cost of multipath losses that prevent detection at certain ranges. However, most geometries exhibit only significant losses (>10 db) over short-range separation intervals, as seen in the figures.

4.9.2 Describing the Reflecting Surface

The surface boundary can be thought of as a combination of a *macro* and a *micro* component. The macro component is described as a smooth semi-infinite dielectric or conductor with classical EM properties, whereas the micro component is described in terms of roughness and density/orientation. As an example, for a grassy field the macro component would be the general terrain profile of the field, and the micro component would be the detailed structure of grass growing on the field surface. The roughness of the micro feature modifies the ideal nature of the smooth surface boundary. Figure 4-33 shows the decomposition of a real surface structure into these two key components for analysis.

The effect of a smooth surface on a propagating wave is generally described by its Fresnel reflection coefficient. The roughness factors are derived by either discrete modeling or statistical approaches. For statistical approaches these roughness modifiers

FIGURE 4-33 ■ Complex surface boundary decomposed into smooth and roughness factors.

TABLE 4-5 ■ Surface Electrical and Physical Parameters at MMW ($\mu = 1$)

Surface Type	ε_r	σ_+ (mho/m)	σ_h (m)	β_0 (rad)
Mowed grass	10	0.001	0.01	0.1
Tall grass	10	0.001	0.1	0.2
Gravel	4	0.001	0.02	0.3
Asphalt	6	0.001	0.0004	0.36
Brush	4	0.001	0.5	0.1
Snow	2.5	0.001	0.003	0.25
Desert	2.5	0.001	0.003	0.05
Trees	1.5	0.001	1.5	0.2
Sea water	80	4	*	*
Fresh water	67	0.1	*	*

relate to rms height and rms slope of elemental surface facets overlaid upon the smooth surface component [29,30]. Statistical approaches work well for bounding set prediction; however, for higher-fidelity representation of a specific scene, discrete modeling, which digitizes the ray structure on the complex surface, is best. This can be accomplished with discrete ray tracing or method-of-moments (MoM) models such as models TKMOD and MRSim (see Section 4.11).

For multipath analysis, surfaces are generally described in terms of three electrical and two physical parameters: (electrical) permeability, μ; permittivity, ε; conductivity, σ_+; (physical) rms roughness, σ_h; and rms slope, β_0. For most frequencies of interest, these parameters have been measured for specific types of surfaces. Table 4-5, compiled from many sources, lists representative values of these parameters for a number of surface classes at MMW frequencies [31,32]. Note that the permittivity listed is the relative dielectric constant, ε_r, based on the ratio of free-space dielectric to dielectric in the medium. The blank parameters marked "*" are determined from sea-state tables[7] and the relationship between surface correlation length and rms slope. For statistical models of surface features, the spatial correlation length, T, is given by [24]

$$T = \frac{2\sigma_h}{\tan \beta_0} \tag{4.30}$$

The spatial correlation length describes the minimum surface distance from a given point at which the features will have significantly changed. It can be directly measured and is often used to infer the equivalent roughness and slope of a surface. It can also be used to determine terrain sampling requirements when using digital simulations derived from measured elevation data.

Using the concepts discussed, Table 4-6 gives representative values of the physical properties for various sea states. Given a sea state (wave height), the equivalent rms roughness can be estimated. If the wave correlation length is also measured, the rms slope can then be determined from Table 4-6, the roughness, and equation (4.30).

[7] *Sea state* is a measure of rms wave height. See Chapter 5 for more information.

TABLE 4-6 ■ Water Surface Parameters by Sea State (All Wind Values)

Sea State	Type	σ_h (m)	β_0 (rad)
0	Calm	0.0001	<0.0001
1	Smooth	0.0–0.03	0.0353
2	Slight	0.03–1.0	0.3097
3	Moderate	1.0–1.5	0.1368
4	Rough	1.5–2.5	0.1064
5	Very rough	2.5–4.0	0.1021
6	High	4.0–6.0	0.1092
7	Very high	>6.0	0.1273

4.9.3 The Multipath Reflection Coefficient

The Fresnel reflection coefficient, Γ, that describes the effect of the surface on the complex voltage of the reflected wave is a combination of the smooth earth Fresnel reflection, Γ_0, the spherical earth divergence factor, D, and the sum of both specular and diffuse roughness modifier components, ρ_s and ρ_d, respectively. This relationship is

$$\Gamma = \Gamma_0 D(\rho_s + \rho_d) \tag{4.31}$$

Each of the components of Γ is discussed in the following subsections.

4.9.3.1 Fresnel Reflection Coefficients

For most surfaces of interest the Fresnel reflection coefficient, Γ_0, may be expressed for polarization parallel and perpendicular to the plane of incidence (the surface) according to [31]

$$\begin{aligned} \Gamma_0^{VV} &= \frac{Y^2 \sin\gamma - \sqrt{Y^2 - \cos^2\gamma}}{Y^2 \sin\gamma + \sqrt{Y^2 - \cos^2\gamma}} \\ \Gamma_0^{HH} &= \frac{\sin\gamma - \sqrt{Y^2 - \cos^2\gamma}}{\sin\gamma + \sqrt{Y^2 - \cos^2\gamma}} \end{aligned} \tag{4.32}$$

where Y is the boundary admittance and γ is the grazing angle. The boundary admittance is defined as $Y = \sqrt{\varepsilon_{rc}/\mu_{rc}}$, where μ_{rc} is the relative complex magnetic component of admittance and ε_{rc} is the relative complex dielectric constant. In most cases μ_{rc} is simply 1.0. ε_{rc} is given by the combination of the relative dielectric constant, ε_r, and the conductivity, σ_+, as

$$\varepsilon_{rc} = \varepsilon_r + \frac{1}{j\omega\sigma_+} \tag{4.33}$$

where ω is the radian frequency of the wave.

For many surfaces of interest (e.g., desert, sea water, grass), the Fresnel reflection coefficient, Γ_0, is typically -1.0 at lower frequencies on long-range ground-to-ground links.[8] Figure 4-34 demonstrates the computed magnitude and relative phase of the

[8]This is primarily due to Brewster's angle being above the very low grazing angle in these geometries. The phase is based on Stratton's convention [33], where the reflected polarization perpendicular to the boundary (vertical) is 180 degrees out of phase with the incident wave.

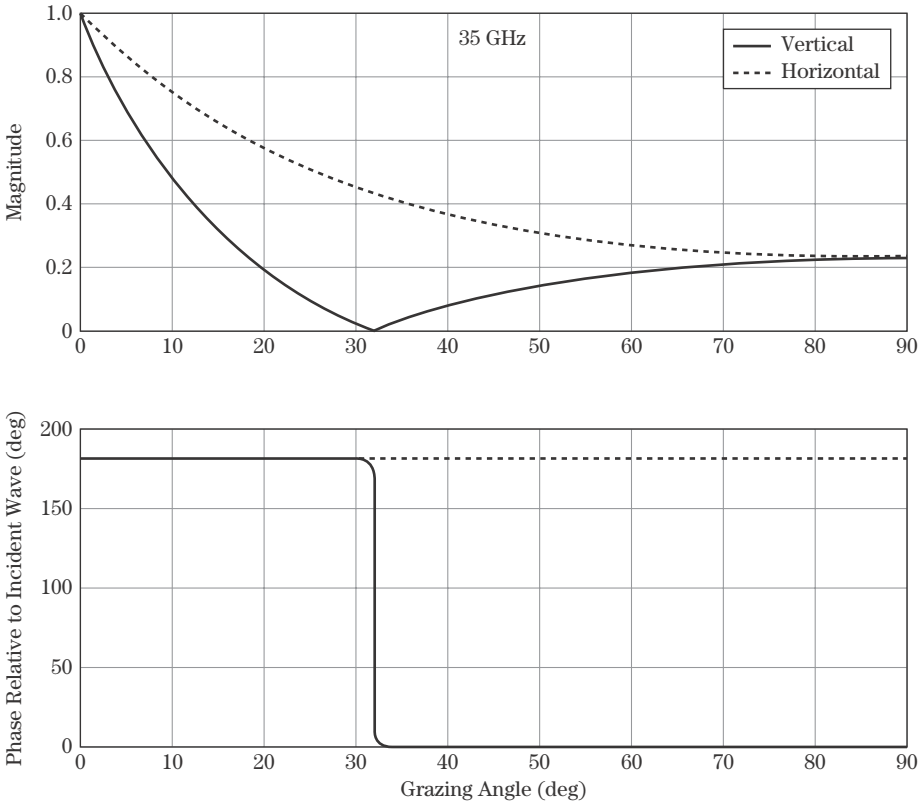

FIGURE 4-34 ■ Fresnel reflection coefficient (magnitude and relative phase) for a desert surface.

reflection coefficient to the incident wave for a desert surface ($\varepsilon_r = 2.5$) at Ka-band for the two linear polarizations.

Based on the Fresnel equations, two key angles are of interest for radar propagation: the critical angle and Brewster's angle. The *critical angle,* θ_c, allows all the energy to be reflected off the boundary layer. When considering long-range communication or OTH radar propagation, both of which operate via one or more reflections off the ionosphere, the critical angle is often used to ensure full reflection off a particular boundary when multipath is in a gain condition. It is given by

$$\theta_C = \sin^{-1}\sqrt{\frac{\varepsilon_2 \upsilon_2}{\varepsilon_1 \upsilon_1}} = \sin^{-1}\sqrt{\frac{\varepsilon_2}{\varepsilon_1}} = \sin^{-1}\sqrt{\varepsilon_r} \tag{4.34}$$

where ε_r is the relative dielectric constant between the two layer boundaries.

Brewster's angle is the grazing angle at which all of the incident energy is transmitted into the boundary with no reflection; there is no multipath field. It is given by

$$\theta_B = \sin^{-1}\sqrt{\frac{\varepsilon_2}{\varepsilon_1 + \varepsilon_2}} = \tan^{-1}\sqrt{\frac{\varepsilon_2}{\varepsilon_1}} = \tan^{-1}\sqrt{\varepsilon_r} \tag{4.35}$$

Brewster's angle is most often exploited for ground-to-ground communications and ground-to-space applications. Since the energy incident on the boundary is not reflected, it cannot interfere with the reception at a receiver. Figure 4-35 plots the critical and Brewster's angles versus relative dielectric constant of the boundary.

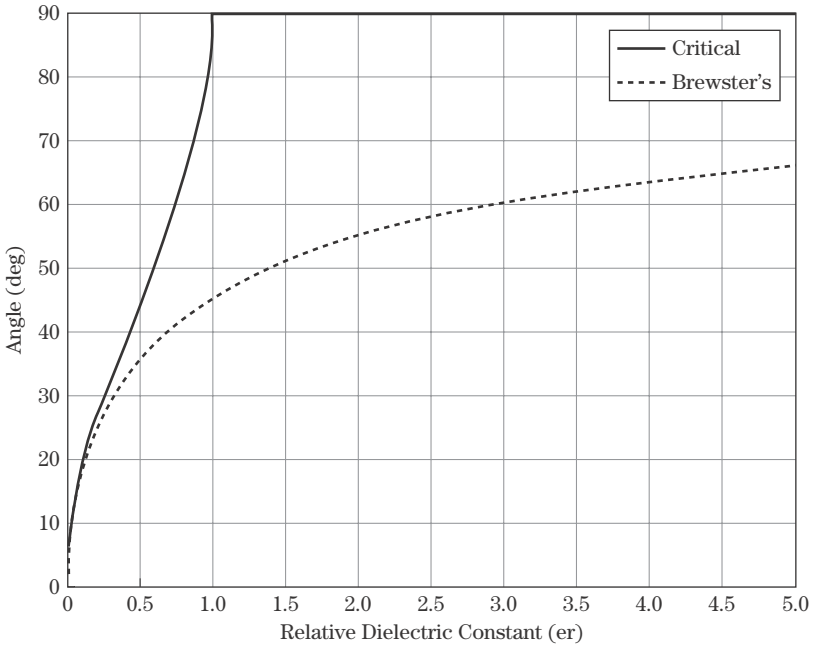

FIGURE 4-35 ■ Key reflection/transmission angles versus relative dielectric constant of the boundary.

In many ground-to-ground engagements, the grazing angle to the surface is much less than 1 degree. In air-to-ground engagements, the grazing angles can vary widely. The angle at which the vertically polarized E-field reflection coefficient reaches zero and the phase changes by 180 degrees is Brewster's angle, discussed earlier. At angles near Brewster's, the incident energy is largely transmitted into the medium, leaving less to be forward scattered to form a multipath ray. Table 4-7 provides the value of Brewster's angle for several terrain types at 35 GHz.

For grazing angles below those listed, no circular polarization sense change is observed in the scattered field. However, the closer the grazing angle is to Brewster's angle, the more the vertically polarized scattered component is attenuated, thus causing an imbalance between the V and H vector components of a circularly polarized incident wave and converting the scattered wave to elliptical polarization. For grazing angles above Brewster's, circular polarization sense flips on the reflected wave such that right-handed circular (RHC) becomes left-handed circular (LHC) and vice versa.

TABLE 4-7 ■ Computed Brewster's Angle for Selected Surfaces at 35 GHz

Surface Type	Brewster's Angle (Grazing; in Degrees)
Desert	32.3
Grass	17.5
Gravel	26.6
Snow	32.3
Sea water	6.4
Perfect conductor	0.0 (e.g., sheet of metal)

4.9.3.2 Divergence Factor

When a radar beam is reflected off a flat, perfectly conductive surface, it can be argued that the amplitude of the reflected beam equals that of the incident beam. This means that a direct and indirect ray arriving at a target will have approximately the same power. This is not the case when the reflection occurs on a smooth spherical surface, such as when a radar beam is reflected off a smooth, calm sea. Due to the curvature of the spherical surface, the reflected waves will diverge instead of following a parallel path, as seen in Figure 4-36. Therefore, the divergence factor, D, is incorporated to account for this beam divergence.

For the geometry defined in Figure 4-36, where the grazing angle, ψ, is assumed small such that $\sin(2\psi) \approx 2\psi$, it can be shown that

$$\psi \approx \frac{1}{r_1}\left[h_1 - \frac{r_1^2}{2a_e}\right] \tag{4.36}$$

This approximation for ψ can be used in an expression for D given by Kerr [24], p. 99, to obtain

$$D \approx \left[1 + \frac{2r_1^2(r - r_1)}{a_e r\left(h_1 - \left(r_1^2/2a_e\right)\right)}\right]^{-1/2} \tag{4.37}$$

which is valid for small grazing angles, ψ.

Most radar applications involve ranges that do not exceed the standard atmosphere radar horizon. For these applications, the impact of the divergence factor is negligible (e.g., $D \approx 1$). In very long-range applications, the curvature of the earth can have a

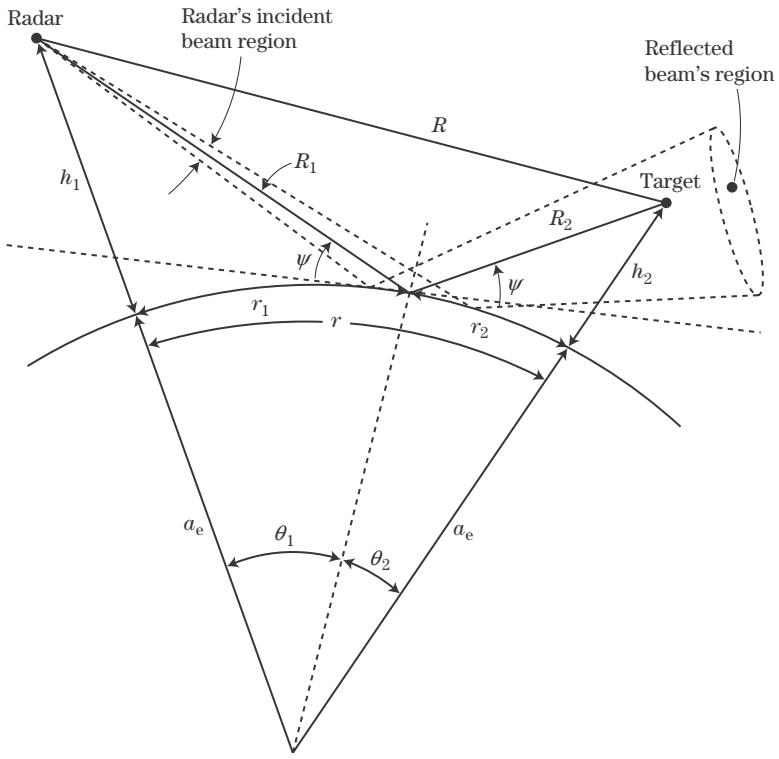

FIGURE 4-36 ■ Geometry for reflections from a spherical, smooth earth.

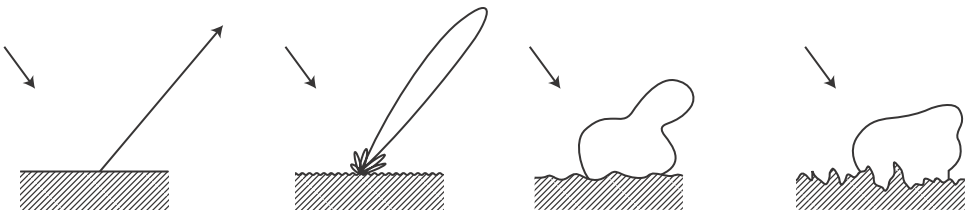

FIGURE 4-37 ■ Illustration of specular to diffuse scattering transitions with increasing surface roughness.

significant impact on the total reflection coefficient. This impact, coupled with a rough, curved surface, yields a more complex situation more fully described in Beckmann and Spizzichino [34].

4.9.3.3 Roughness Factors

The roughness factors, ρ_s and ρ_d, modify the reflection coefficient, Γ, as shown in equation (4.31). Specular scattering is generally described as a point reflection at Snell's angle from the intermediate surface. Diffusely scattered fields emanate from a spatially distributed area known as the *glistening surface* and decorrelate more rapidly than the "coherent" specular terms. Diffuse interference typically does not cause persistent signal fades but has been shown to contribute residual error in track processors.

As surface roughness increases, the dominant scattered wave transitions from specular to diffuse (Figure 4-37). In specular scattering, the reflected wave is a close replica of the incident wave and can cause coherent interference patterns at the receiver. In the limit, diffuse scattering is nearly hemispherical (also known as a *Lambertian reflectance*, or scattering in the case of light) but with lower gain in any particular direction (i.e., a fuzzy replica of the incident wave). Diffuse energy thus tends to "splatter" over a broader region of angle space.

Conservation of energy dictates that, when specular reflection is reduced, diffuse energy becomes more significant in the scattered field and also implies that surface roughness is increasing. In general, specular multipath occurs when the surface roughness is small compared with the wavelength and diffuse multipath becomes significant when roughness is higher compared with the wavelength. Beckmann and Spizzichino [34] observed that in the limit for nondirectional antenna, the maximum value of the diffuse roughness factor, ρ_d, is 0.5. Figure 4-38 illustrates the magnitude of the specular and diffuse roughness factors as a function of normalized roughness. The normalized surface rms roughness value, σ_h', takes into account the perceived roughness at a specific radar frequency and the grazing angle according to

$$\sigma_h' = \frac{\sigma_h}{\lambda} \sin \gamma \tag{4.38}$$

Specular Scattering The specular field is essentially a scaled replica of the transmit signal delayed by $\Delta R/c$ seconds. The amplitude of the specular roughness factor ρ_s is given by

$$|\rho_s| = \exp\left(-\frac{4\pi}{\lambda}\sigma_h \sin\gamma\right)^2 = \exp\left(-4\pi\sigma_h'\right)^2 \tag{4.39}$$

The phase of the specular roughness factor, ϕ_s, includes the Fresnel term and a term due to the extra path length,

$$\phi_s = \phi_{Fresnel} + k\delta R \tag{4.40}$$

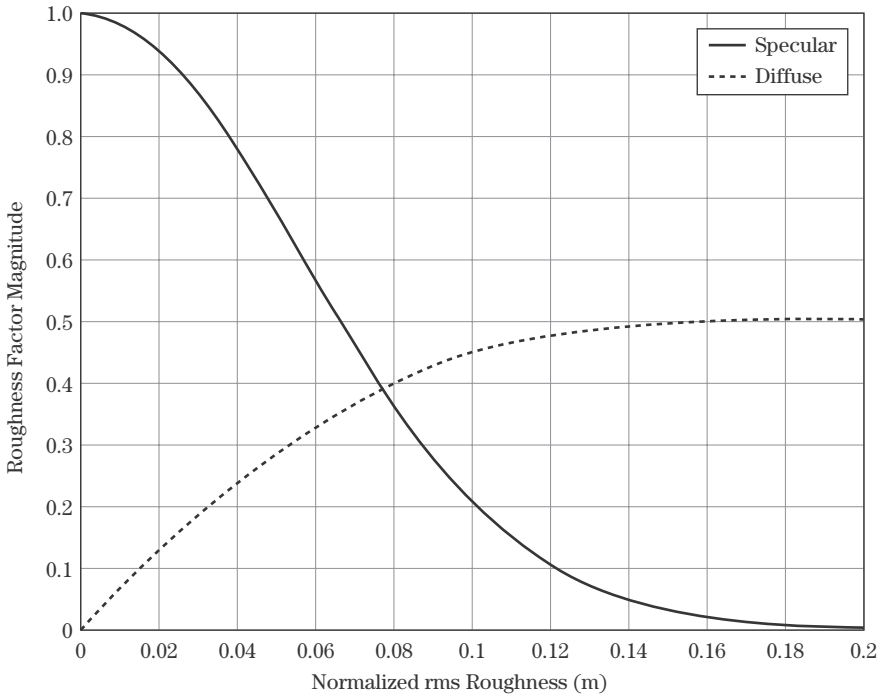

FIGURE 4-38 ■ Specular and diffuse roughness factor transition versus normalized surface rms roughness.

For temporally varying surfaces (e.g., wind-blown trees, water), the specular roughness factor should not be modeled as a constant but as a pseudo-random process that captures the temporal, spatial, and frequency decorrelation statistics appropriate for the surface type. The power spectrum is generally modeled as a low-pass function with a cutoff frequency, ω_c, determined from the decorrelation time, T, according to

$$\omega_c = \frac{2\pi}{T} \tag{4.41}$$

An example of measured autocorrelation functions for scattered field amplitude from a moving terrain (nominal sea condition) is given in Figure 4-39. Additional examples of clutter correlation statistics are given in Chapter 5. The decorrelation point is generally considered to be the time lag at which the normalized autocorrelation function first falls to a value of $1/e$, or about 10% of its original amplitude. In Figure 4-39, the decorrelation time is evidently on the order of 1 second.

Diffuse Scattering The magnitude of the diffusely scattered field is computed from the geometry, rms surface roughness, and slope parameters. Because of conservation of energy, the magnitude of the diffuse reflection coefficient will be limited by the specular reflection magnitude [36]. Based on this conservation principle and the maximum values observed for diffuse scatter in the presence of a strong specular field [34], the magnitude of the diffuse roughness factor contribution (in the limit) can be approximated by

$$\left|\rho_{d_{\text{limit}}}\right| = 0.5\sqrt{(1 - |\rho_s|)} \tag{4.42}$$

This value was used to estimate the diffuse magnitude as a function of specular magnitude in Figure 4-38. Consider the geometry shown in Figure 4-40. The nominal

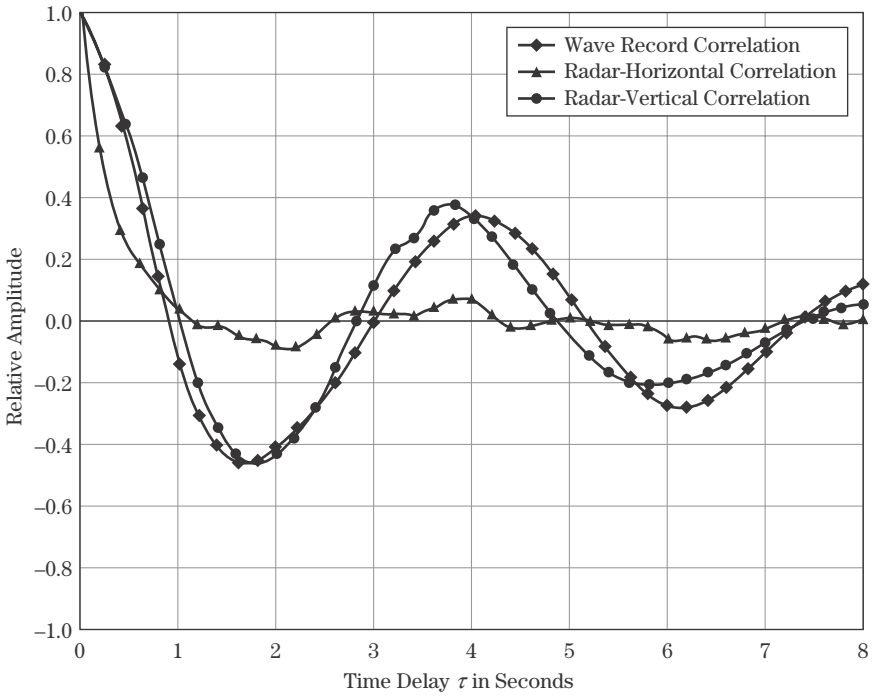

FIGURE 4-39 ■ Decorrelation data from nominal sea/wind condition. (From Meyers [35]. With permission.)

Hydrographic – Nov 12	**Statistical**
Wave Height – 1.4 Ft.	**Radar - Vertical**
Period – 2.9 Sec.	Range – 430 YD, AZ–095 Deg.
Velocity – 9.7 Ft./Sec.	Tilt – 1.5 to 4.2 Deg., HT – 33 to 93 Ft.
Wavelength – 28 Ft.	AV. Power – 4.07 Microwatts
Direction – 045 Deg.	**Radar - Horizontal**
	Range, Azimuth – Same
	Tilt, Height – Same
	AV. Power – 1.53 Microwatts
	Wave Record
	Standard Deviation – 0.524 Ft.
	Significant Wave Height – 2.3 Ft.

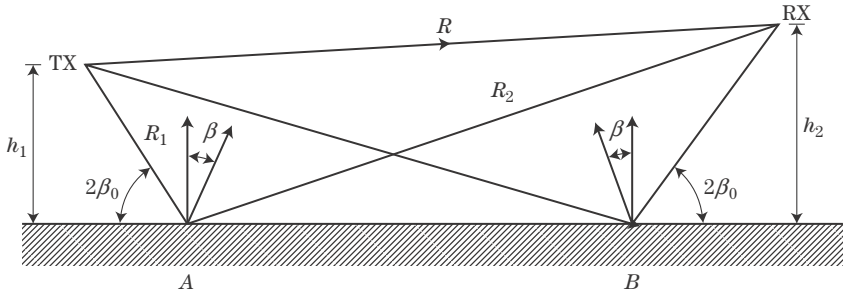

FIGURE 4-40 ■ Diffuse primary scattering geometry.

component amplitudes for each of the diffuse roughness factors, $\rho_{d_{1,2}}$, are approximated by [34]

$$\left|\rho_{d_{1,2}}\right| = \frac{R^2}{R_1^2 R_2^2 \tan^2 \beta_0} \exp\left(\frac{\tan^2 \beta}{\tan^2 \beta_0}\right) \tag{4.43}$$

where β is the difference between the surface normal and bisector angle of the incident and reflected rays (R_n,R_{n+1}), and β_0 is the rms surface slope parameter.

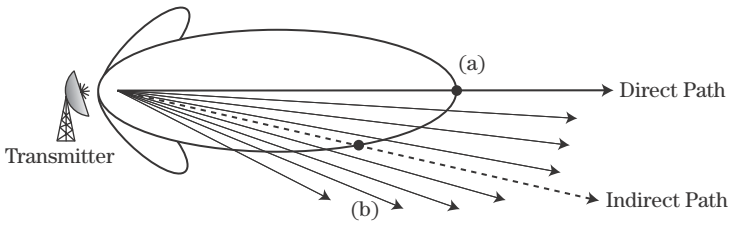

FIGURE 4-41 ■ Ratio of antenna gains at direct and indirect path angles.

The phase of the diffuse energy is based on the extended path length to two primary reflection points (points A and B in Figure 4-40) directly in front of the transmitter and receiver. The effects of the antenna gain pattern must also be included in the computation of amplitude and phase for scattered rays at the appropriate indirect angles. Similar to the specular reflection case, a random process model is needed to account for temporal decorrelation of each diffuse reflection component.

4.9.3.4 Angle Error

Specular multipath is a source of angle error biases. For a monopulse tracking system (see Chapter 18), these bias errors decorrelate very slowly and can lead to significant residual errors in the tracking filter. On the other hand, a shorter wavelength causes associated increases in diffuse multipath contributions that can be significantly reduced (but not eliminated) by simple temporal integration or averaging. Similar results can occur with narrow-band Doppler filtering. In low-angle applications where the tracker illuminates both the true target and the virtual target created by the indirect paths, the indicated angle is that of the equivalent two-scatterer target of Figure 4-29. In these cases the rms angle error caused by multipath can be computed from [36]

$$\sigma_{rms} = \frac{\rho_s \theta_3}{\sqrt{8 G_{se}(\text{peak})}} \tag{4.44}$$

where θ_3 is the one-way 3 db beamwidth of the tracking antenna, and G_{se}(peak) is the ratio of the antenna gains for the direct path target and the indirect path image at angles shown in Figure 4-41a and Figure 4-41b.

Angle errors due to specular multipath reflection are summarized for two example surface roughness values in Table 4-8 for a low-angle ground-to-ground geometry where the aperture size was limited to 5.5 inches.[9] When the terrain is very smooth, all the system "sees" is a very high specular reflection. As the surface roughness increases, the higher frequency systems see the earth as an increasingly rough surface, thus reducing the magnitude of specular reflections and associated error biases. Multipath usually impacts only the elevation plane with angle errors, although diffuse multipath, which emanates from a wider surface area, can induce residual errors into the azimuth plane.

4.9.3.5 Classification Error

The presence of additional target images at range delays δR can also cause the true target to have an extended length, which can cause problems for classifiers using target length as a discriminant. For the one-way case, a replica of the true target will exist at a range

[9]This aperture size produces a 3 dB one-way beamwidth of 13 degrees at 10 GHz and 3.6 degrees at 35 GHz.

TABLE 4-8 ■ Elevation Angle Error for Two Frequencies and Surface Roughness Values ($G_{se}(\text{peak}) = 1$)

Roughness	10 GHz	35 GHz
0.1 m	67.2 mr	21.1 mr
1.0 m	66.5 mr	19.6 mr

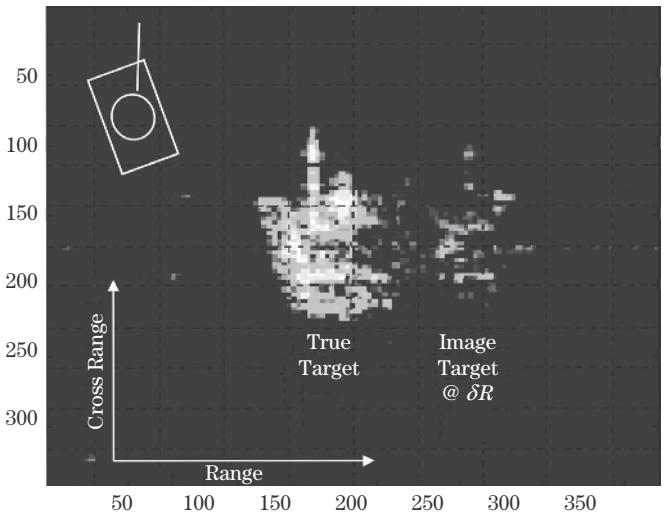

FIGURE 4-42 ■ ISAR image of a tank located over a smooth surface.

delay of δR. For the two-way case, replicas of the true target will exist at range delays of δR and $2\delta R$. The replica at δR for the two-way case can also be larger in amplitude than the true target if the reflection coefficient on the surface is high. For a distributed target (e.g., ships, tanks), each dominant scatterer may have these replicas causing the scatterer distribution to significantly change over free space. Figure 4-42 illustrates the distribution of two-dimensional scatterers on a tank target at 35 GHz and the ghost image created by the multipath bounce at range delay δR. For this two-way geometry, the third image located at $2\delta R$ is below the threshold of the gray scale, indicating that the reflection coefficient was below 0.7 on the surface.

4.10 | SKIN DEPTH AND PENETRATION: TRANSMITTING THROUGH WALLS

Most materials other than metal are poor conductors to radar waves, and, instead of the waves being reflected, the waves will penetrate into or through the material. *Skin depth* describes how far a signal penetrates past a boundary and into a material. When applied to the transmission of EM waves through walls, ground,[10] and other obstacles, it is customary

[10]Ground-penetrating radar (GPR) is another application in which these principles apply. GPR systems generally use a specialized waveform (impulse approximations or monocycles) to maximize energy into the medium.

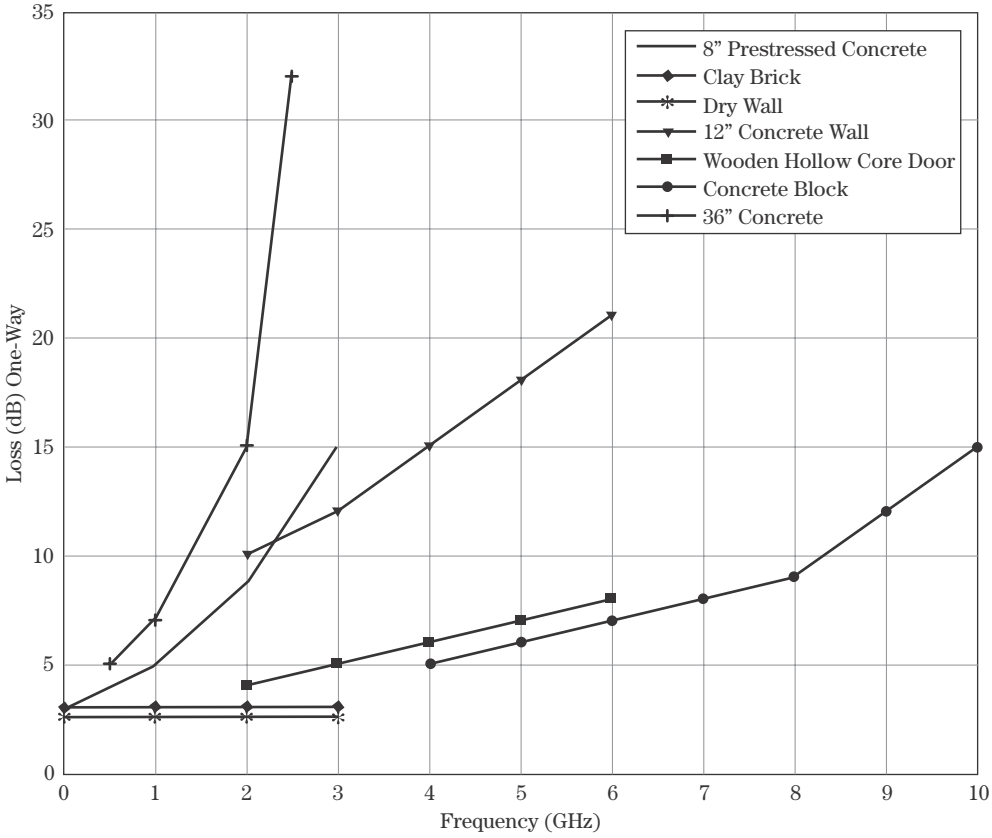

FIGURE 4-43 ■ Radar wave penetration through some standard materials.

to define the skin depth or depth of penetration, δ, as that distance at which the transmitted wave intensity has been attenuated to $1/e$ of its value at the wall surface.

For "good conductors" the skin depth or penetration of the wave at normal incidence is

$$\delta = \sqrt{\frac{2}{\omega\mu\sigma_+}} = \sqrt{\frac{1}{\pi f \mu \sigma_+}} \tag{4.45}$$

where f is the frequency (Hz), μ is the material's permeability (H/m), and σ_+ (S/m) is the material's conductivity. A number of material properties useful for computing skin depth have been compiled by Neff [37]. If the skin depth is greater than the thickness of the material, then the attenuated wave will exit the boundary into the next medium.

Data on the penetration of radar waves into different material types and thicknesses have been published in a number of references, most notably in [38-41]. Figure 4-43 shows attenuation versus carrier frequency for several common wall materials. As expected, the losses generally increase with higher frequency.

While in the medium, the radar wave will slow down due to the refractive index change. The phase velocity in the medium is given by

$$v_p = \frac{c}{n} \tag{4.46}$$

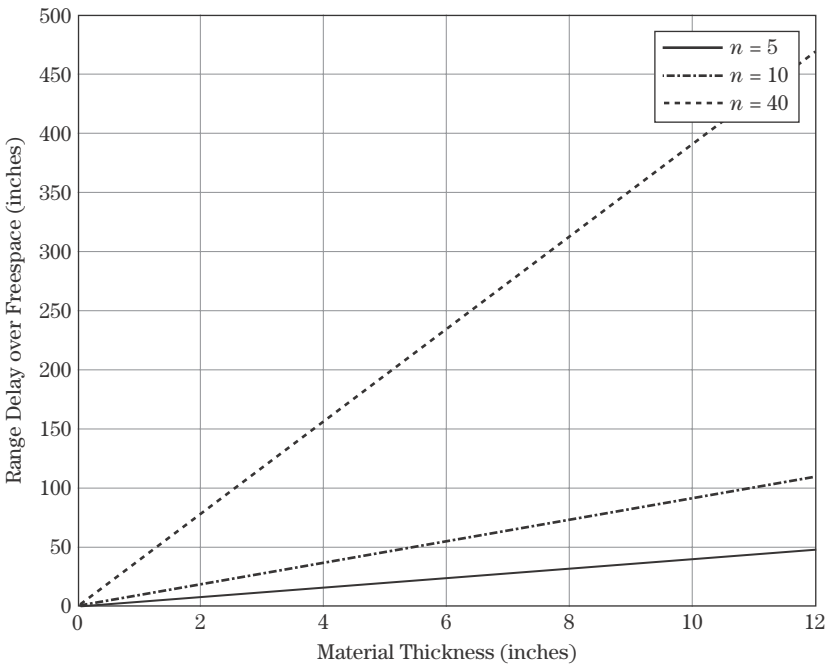

FIGURE 4-44 ■ Radar wave range delay through boundary materials with three refractive indexes.

where c is the speed of light (free-space phase velocity, or 3×10^8 m/s), and n is the refractive index of the material. Thus, the thicker the material and the higher the refractive index, the longer the propagation time through the material. Figure 4-44 illustrates the additional time (range) delay of a wave propagating through a material of various thicknesses for three refractive indexes.

This effect can be quite substantial. The more material in the path, the more delay is incurred by the propagating wave. This is a difficult obstacle for time of arrival measurement systems that must see through many walls into buildings.

4.11 COMMERCIAL SIMULATIONS

Numerous currently available computer models in government and industry may be subjectively classified as off the shelf or developmental. Following is a list of a number of such models, with links to websites providing more information on these simulations:

- TIREM (Terrain Integration Rough Earth Model)
  http://www.alionscience.com
- LEIBE MPM (Microwave Propagation Model)
  http://adsabs.harvard.edu/abs/1989IJIMW..10..631L
- TKMOD5C
  http://www2.electronicproducts.com/PrintArticle.aspx?ArticleURL=CAERP5.NOV1994
- COMBIC (Combined Obscuration Model for Battlefield-Induced Contamination)
  http://www.ontar.com
- XPatch
  http://www.saic.com/products/software/xpatch/

TABLE 4-9 ■ Propagation Model Utility and Fidelity Assessment Matrix

Model Name	Atmos Atten	Atmos Refraction	Atmos Turbulence	Surface Intervisibility	Surface Diffraction	Surface Multipath
TIREM	◑	○	○	◑	●	◑
LEIBE MPM	●	○	◑	○	○	○
TKMOD5C	◑	○	○	●	○	●
COMBIC	◑	◑	◑	○	○	○
XPatch	◑	○	○	●	◑	◑
MRSIM	◑	○	○	●	○	●
EREPS	◑	●	○	○	○	○
TEMPER	●	●	○	○	○	○
PCPEM	●	●	○	○	○	○

- MRSIM (Multispectral Response Simulation)
  http://resrchnet.com/products.htm
- EREPS (Engineering Refractive Effects Prediction)
  http://areps.spawar.navy.mil/2858/software/ereps/readerep.txt
- TEMPER (Tropospheric Electromagnetic Parabolic Equation Routine)
  http://www.jhuapl.edu/techdigest/td2502/Awadallah.pdf
- PCPEM (Personal Computer Parabolic Equation Model)
  http://www.nat-hazards-earth-syst-sci.net/7/391/2007/nhess-7-391-2007.pdf

In most cases, closed-form solutions include a number of limiting assumptions and are generally thought to be rules of thumb for quick analysis insight. Many current codes combine closed-form solutions with digital terrain and wave representations.

Table 4-9 attempts a rating of the tools based on algorithm level of fidelity for each propagation mechanism. This matrix is not intended to be complete, nor does it indicate an endorsement or criticism of each code. It is provided only to demonstrate numerous options to the reader for assessments of mechanism impacts in more complicated scenarios. Note that all the probable mechanisms are covered by at least one of the identified models. For each of the mechanisms, one of three rating levels is listed:

- ○ **No Support for Mechanism:** The simulation doesn't predict or incorporate effects of the propagation mechanism at all.
- ◑ **Low/Medium Fidelity:** The simulation or model uses rule-of-thumb solutions and presumes homogenous or uniform distributions and occurrences throughout the medium. Phenomenological variants are represented in a similar manner.
- ● **High Fidelity:** The simulation or model uses discrete models or series expansions to closely emulate the physics of a particular mechanism (e.g., MoMs, geometric optics) and can support multiple variants of a basic phenomenology.

In all of these cases, validation data of significant volume are not present to completely assess the accuracy of indicated codes. Most models are validated only against "idealized" measurement data over a few conditions since no generalized approach completely predicts anomalies in the measured data.

For additional propagation models, visit either the website of the International Telecommunications Union (http://www.itu.int), which contains many propagation models suitable for a variety of applications, or the European Communications Office

(http://www.ero.dk/seamcat), which has a free download of a Monte Carlo method for propagation modeling and simulation and analysis.

4.12 SUMMARY AND FURTHER READING

This chapter addresses most, but not all, key propagation mechanisms; a number of other mechanisms and techniques not discussed include the following:

1. Atmospheric emission. Atmospheric constituents produce thermal emissions that increase the background noise temperature. The thermal emission is proportional to the absorption due to, for example, atmospheric gases, rain, clouds, fog, dust, and smoke. Emission must be taken into account not only along the path between the radar and the target but beyond the target as well. This effect depends on the frequency and elevation angle as well as on the absorber characteristics and temperature. An increase in the background noise temperature (i.e., "sky noise") can affect the performance of surface-based air surveillance, space surveillance, and ballistic missile defense radars.
2. Surface wave propagation. Surface wave (or ground wave) propagation is used by some HF radars to provide coverage to ranges well beyond the conventional radar horizon but short of the coverage provided by ionospheric propagation. Such coverage extends into the coverage gap known as the ionospheric "skip zone."
3. Ground-penetrating radar. There has been considerable research and development activity in the area of ground-penetrating radar in the last 10–15 years, including some commercial applications. Radar has also been used to probe the ice sheets of Greenland and Antarctica to depths of several kilometers. In addition, two subsurface radar sounders (VHF and UHF) are in orbit around Mars. Propagation in soil or ice presents some unique issues and challenges.
4. Atmospheric turbulence sensing. There has been considerable research and development activity in the area of sensor fusion (MMW radar and LADAR) combining to detect clear air turbulence phenomena for aircraft.
5. Trans-ionospheric propagation. Space-based radars are becoming more common in both civil remote sensing and military applications. Surface-based ballistic missile defense radars may be required to detect targets outside the atmosphere. Both of these applications must use trans-ionospheric propagation paths. Ionospheric effects can degrade the measurement accuracy of several parameters including range delay, direction of arrival, and polarization.

In addition to the books on propagation listed in the reference section [3,7,20,24,34], some additional texts are recommended for further reading and investigation for readers both new and old to the subject. Each has many strong points to recommend, and, depending on readers' specific interests, should provide a good starting point for getting into the literature of radar propagation.

Blaunstein and Plohotniuc [50] is recommended for those needing a detailed background in propagation associated with the ionosphere. It is more specific and at a much deeper level than the other books listed here. Blaunstein and Christodoulou [51] is a very complete book. Despite its orientation toward wireless communications, its core material is also useful for radar propagation and covers several topic areas the other recommended texts do not, such as statistical variations in propagation models.

Seybold's book [52] not only covers the basics of RF propagation but is also an especially good introduction to the variety of modeling techniques for RF propagation. Barclay [53] provides a very complete text on RF propagation, at a more detailed level than most of the other recommended books. There is good coverage of several of the key recommendations for further reading on propagation.

An excellent one-book compilation covering the impact of land and sea on radar propagation, covering not only the usual effects of reflection, refraction, and diffraction but also the impact of clutter on radar returns is Long [54]. Lavergnat and Sylvain [55] give a good introduction to RF propagation, with many worked examples for those wanting to get a feel for the quantities involved in propagation problems. Last but not least, Shibuya's [56] book, although older, is very complete and comprehensive.

4.13 REFERENCES

[1] Burge, C.J., and Lind, J.H., *Line-of-Sight Handbook,* Naval Weapons Center, NWC-TP-5908, January 1977.

[2] Eaves, J.L., and Reedy, E.K., *Principles of Modern Radar,* Van Nostrand Co., New York, 1987.

[3] Bogush, A.J., *Radar and the Atmosphere,* Artech House, Norwood, MA, 1989.

[4] Battan, L.J., *Radar Characteristics of the Atmosphere,* University of Chicago Press, Chicago, 1973.

[5] Austin, P.M., "Radar Measurements of the Distribution of Precipitation in New England Storms," Proceedings of the 10th Weather Conference, Boston, 1965.

[6] P-N Designs, Inc., *Electronic Warfare and Radar Systems Handbook,* http://www.microwaves101.com/encyclopedia/Navy_Handbook.cfm

[7] Nathanson, F., Radar Design Principles, 2d ed., Scitech, Raleigh, NC, 1999.

[8] Richard, V.M., Kammerer, J.E., and Reitz, R.G., "140-GHz Attenuation and Optical Visibility Measurements of Fog, Rain, and Snow," ARBRL-MR-2800, December 1977.

[9] Nakaya, U., and Terada, T., "Simultaneous Observations of the Mass, Falling Velocity, and Form of Individual Snow Crystals," *Journal of the Faculty of Science,* vol. 1, no. 7, pp. 191–200, 1935.

[10] Perry, B.P, et al., "Effects of Smoke on MMW Radar Measurements," GTRI Final Technical Report A-9007, July 1992.

[11] Pedersen, N.E., Waterman, P.C., and Pedersen, J.C., "Absorption Scattering and Thermal Radiation by Conductive Fibers," AFOSR Final Report, Panametrics, Inc., July 1987.

[12] *U.S. Standard Atmosphere, 1976,* U.S. Government Printing Office, Washington, DC, 1976. Available at: http://ntrs.nasa.gov/archive/nasa/casi.ntrs.nasa.gov/19770009539_1977009539.pdf

[13] ICAO, *Manual of the ICAO Standard Atmosphere*, Doc 7488-CD, 3d ed., 1993.

[14] International Organization for Standardization (ISO), "Standard Atmosphere," *ISO,* vol. 2533, p. 1975, 1975.

[15] Berkowitz, R.S., *Modern Radar Analysis, Evaluation and System Design,* Wiley & Sons, New York, 1965.

[16] Bean, B.R., and Dutton, E.J., "Radio Meteorology," NBS Monograph 92, U.S. Department of Commerce, 1965.

[17] Barton, D.K., *Modern Radar System Analysis*, Artech House, Norwood, MA, 1988.

[18] Ko, H.W., Sari, J.W., and Skura, J.P., "Anomalous Microwave Propagation through Atmospheric Ducts," *Johns Hopkins APL Technical Digest,* vol. 4, no. 1, pp. 12–26, 1983.

[19] Skolnik, M.I., *Introduction to Radar Systems,* 3d ed., McGraw-Hill Co., New York, 2001.

[20] Skolnik, M.I., *Radar Handbook,* 3d ed., McGraw-Hill Co., New York, 2008.

[21] "Engineering Refractive Effects Prediction System (EREPS)," http://areps.spawar.navy.mil/2858/software/ereps/readerep.txt

[22] Bohlander, R.A., McMillan, R.W., Patterson, E.M., Clifford, S.F., Hill, R.J., Priestly, J.T., et al., "Fluctuations in Millimeter-Wave Signals Propagated through Inclement weather", *IEEE Transactions on Geoscience and Remote Sensing,* vol. 26, no. 3, pp. 343–354, 1988.

[23] Churnside, J.H., and Lataitis, R.J., "Angle-of-Arrival Fluctuations of a Reflected Beam in Atmospheric Turbulence," *Journal of the Optical Society of America,* vol. 4, pp. 1264–1272, July 1987.

[24] Kerr, D.E., *Propagation of Short Radio Waves,* McGraw-Hill, New York, 1951.

[25] Sommerfield, A.J., *Optics*, Academic Press, Inc., New York, 1954.

[26] Keller, "Diffraction by a Convex Cylinder," *IRE Transactions on Antennas and Propagation,* vol. 4, no. 3, pp. 312–321, July 1956.

[27] Keller, J.B., "Geometrical Theory of Diffraction," *Journal of the Optical Society of America,* vol. 52, no. 2, February 1962.

[28] IEEE Standard Radar Definitions, IEEE Std 686-1982, Institute of Electrical and Electronic Engineers, New York, 1982.

[29] Saffold, J.A., and Tuley, M.T., "A Multidimensional Terrain Model for Low Altitude Tracking Scenarios," 1990 Summer Computer Simulation Conference (SCS), Calgary, Alberta Canada, July 18, 1990.

[30] Bruder, J.A., and Saffold, J.A., "Multipath Effects on Low Angle Tracking at Millimeter Wave Frequencies," *IEE Proceedings of the Radar and Signal Processing: Special Issue on Radar Clutter and Multipath Propagation,* vol. 138, no. 2, pp. 172–184, April 1991.

[31] Ewell, G.W., and Reedy, E.K., "Multipath Effects on Direct Fire Guidance," GTRI Final Technical Report, CR-RD-AS-87-10, June 1987.

[32] Bullington, K. "Reflection Coefficients of Irregular Terrain," *Proceedings of the IRE,* vol. 42, no. 8, pp. 1258–1262, August 1954.

[33] Stratton, J.A., "Electromagnetic Theory," McGraw-Hill, New York, 1941.

[34] Beckmann, P., and Spizzichino A., *The Scattering of Electromagnetic Waves from Rough Surfaces,* Artech House, Norwood, MA, 1987.

[35] Myers G.F. "High Resolution Radar, Part IV, Sea Clutter Analysis," Naval Research Laboratory Report 5191, October 21, 1958.

[36] Barton, D.K., "Low-Angle Radar Tracking," *Proceedings of the IEEE,* vol. 62, no. 6, pp. 687–704, June 1974.

[37] Neff, H., *Basic Electromagnetic Fields,* Harper & Row Publishers, New York, 1981.

[38] Hunt, A.R., and Hogg, R.D., "A Stepped Frequency, CW Radar for Concealed Weapons Detection and Through the Wall Surveillance," *Proceedings of the SPIE,* vol. 4708, 2002.

[39] Falconer, D.G., Ficklin, R.W., and Konolige, K.G., "Robot Mounted Through-Wall Radar for Detecting Locating and Identifying Building Occupants," *Proceedings of the 2002 IEEE International Conference on Robotics and Automation,* vol. 2, pp. 1868–1875, April 2002.

[40] Hunt, A., and Akela Inc., Briefing, "Image Formation through Walls Using a Distribution RADAR Sensor Network," CIS Industrial Associated Meeting, May 12, 2004.

[41] Stone, W.C., "Surveying through Solid Walls," National Institute of Standards and Technology (NIST) paper, Automations Robotics and Construction 14th International Symposium Proceedings, June 8–11, 1997, Pittsburg, PA.

[42] Leubbers, R., "Propagation Prediction for Hilly Terrain Using GTD Wedge Diffraction", *IEEE Transactions on Antennas and Propagation,* vol. AP-32, no. 9, pp. 951–955, September 1984.

[43] Leibe, H.J. "MPM—An Atmospheric Millimeter-Wave Propagation Model," *International Journal of Infrared and Millimeter Waves,* vol. 10, no. 6, June 1980.

[44] Queen, J.L., Stapleton, J., Kang, S., and the Army Infantry School Fort Benning GA Directorate of Combat Development, "Wideband Low-Elevation Microwave Propagation Measurements," Dahlgren Division, NSWC, NSWCDD/TR-95/18, February 1995.

[45] Reed, R., *Ultrahigh Frequency Propagation,* Chapman and Hall, Ltd., London, 1966.

[46] Currie, N.C., Dyer, F.B., and Hayes, R.D., "Analysis of Rain Return at Frequencies of 10, 35, 70, and 95 GHz", Technical Report No. 2, Contract DAA25-73-0256, Georgia Institute of Technology, Atlanta, March 1975.

[47] Pasquill, F., and Smith, F.B. (Ed.), *Atmospheric Diffusion*, 3d ed., Ellis Horwood Series in Environmental Science, 1983.

[48] Kobayashi, H.K., "Atmospheric Effects on Millimeter Radio Waves," Atmospheric Science Lab, NM, ASL-TR-0049, January 1980.

[49] Kobayashi, H.K., "Effect of Hail, Snow, and Melting Hydrometeors on Millimeter Radio Waves," Atmospheric Science Lab, NM, TR-0092, July 1981.

[50] Blaunstein, N., and Plohotniuc, E., *Ionospheric and Applied Aspects of Radio Communication and Radar,* Nathan CRC Press, Boca Raton, FL, 2008.

[51] Blaunstein, N., and Christodoulou, C.G., *Radio Propagation and Adaptive Antennas for Wireless Communication Links,* John Wiley & Sons, New York, 2007.

[52] Seybold, J., *Introduction to RF Propagation,* Wiley-Interscience, New York, 2005.

[53] Barclay, L., *Propagation of Radiowaves,* 2d ed., The Institution of Engineering and Technology, London, 2003.

[54] Long, M.W., *Radar Reflectivity of Land and Sea,* 3d ed., Artech House, Norwood, MA, 2001.

[55] Lavergnat, J., and Sylvain, M., *Radiowave Propagation,* John Wiley & Sons, New York, 2000.

[56] Shibuya, S., *A Basic Atlas of Radio-Wave Propagation,* Wiley-Interscience, New York, 1987.

4.14 | PROBLEMS

1. In a specific application the low-frequency (VHF/UHF) radar wave must propagate through continuous rain (high humidity) while remaining low to the earth's surface. The surface is very smooth (low rms roughness) and extends for great distances. Which propagation mechanisms are likely the most significant?

2. There are three significant mechanisms in a two-way path between the radar transmitter and receiver. The presence of multipath provide a propagation factor of 0.8, while atmospherics (rain and fog) provide factors of .95 and .99, respectively. What is the total propagation factor for the path?

3. A 1 watt EM wave of frequency 1 GHz travels through free space at the speed of light (3×10^8 m/s) from a source for a time of 10 μsec. What is the distance traveled and the total phase change (in radians) the wave has traversed?
4. An EM wave travels through a heterogenous atmosphere with rain, fog, and clear air. For each type the distances are 2 km for rain, 1 km for clear air, and 2 km for fog. The attenuation for each of these types is listed as 1 db/km, 0.3 db/km, and 0.7 db/km two-way, respectively. What is the total one-way propagation factor for this path in db?
5. What is the one-way attenuation from clear air at standard atmosphere for a 10 GHz radar at atmospheric temperature 273.15 Kelvin and 59% humidity?
6. What is the attenuation for a 10 GHz radar signal traveling 10 km with a 2 km dust cloud in its path? The dust cloud has a 1.0 extinction efficiency and a concentration of 0.0001 g/m^3 in the 2 km area.
7. What are the general criteria for an edge classification as a "knife" or "rounded tip"?
8. Which edge classification provides the lowest scattered energy in the shadow zone and interference regions?
9. What is the magnitude of the diffracted wave off a $\lambda/10$ radius of curvature knife edge when the incident wave has magnitude 1 and a 15 degree shadow angle from the edge?
10. Which linear polarization component offers a reduction in multipath scattering due to Brewster's angle?
11. What is the spatial correlation length of a rough surface with rms slope of 0.1 degrees and rms roughness of 0.1 meters?
12. When a transmitter and receiver (or target) are at low altitude, long range, and smooth intermediate surface, which roughness component dominates the reflection coefficient?
13. What are the specular reflection angle and range delay values for a transmitter located at 2 meters altitude and a receiver located at 4 meters altitude in a one-way link geometry when the two are separated by 100 meters?
14. Using conservation of energy principles on the roughness factors, what is the magnitude of the diffuse term if the specular reflection coefficient is 0.7?
15. What is the maximum received signal amplitude gain when the geometry is setup to coherently add all two-way reflection components from a 1 watt transmitter?
16. What is the rms angle error in elevation for a tracking radar with a one-way 3 db beamwidth of 2 degrees, a direct/indirect path gain ratio of 0.7, and a ground reflection coefficient of 0.8?
17. For a 5 GHz radar, what is the loss through a single concrete block wall?
18. What is the additional range delay over free space for a wave propagating through two 12 inch thick walls with refractive index of 5?